EFFECT OF IONIC RADIUS OF A-SITE DOPANTS ON THE PHASE TRANSITION TEMPERATURE AND CRYSTAL STRUCTURE OF BISMUTH FERRITE

By

Mohammadreza Khodabakhsh

Submitted to Graduate School of Engineering and Natural Sciences
in partial fulfillment of the degree of Master of Science

SABANCI UNIVERSITY

Jan 2014

EFFECT OF IONIC RADIUS OF A-SITE DOPANTS ON THE PHASE TRANSITION TEMPERATURE AND CRYSTAL STRUCTURE OF BISMUTH FERRITE

APPROVED BY:

Asst. Prof. I. Burc Misirlioglu ……
(Thesis Supervisor)

Prof. Mehmet Ali Gulgun ……

Assoc. Prof. Ali Kosar ……

DATE OF APPROVAL:

13/1/2014

EFFECT OF IONIC RADIUS OF A-SITE DOPANTS ON THE PHASE TRANSITION TEMPERATURE AND CRYSTAL STRUCTURE OF BISMUTH FERRITE

Mohammadreza Khodabakhsh

Material Science and Engineering, M.Sc. Thesis, 2013

Thesis Supervisor: Burç Mısırlıoğlu

Keywords:

Ferroic powders, BiFeO3, phase transitions and structure, defects

Abstract

Doping of ferroics is often intended to generate new functionalities or enhance the already existing properties but it comes at the expense of local structural distortions around dopants in the lattice. We have reported on the effect of A-site doping and their effect on the phase transition temperatures of sol-gel synthesized $Bi_{1-x}A_xFeO_3$ (A: Gd, Sm, La) powders as a function of dopant type and concentration. A clear direct correlation between structural parameters and transition temperatures was noted as a function of ionic radii of dopants for any given concentration, implying the effect of inhomogeneous lattice strains around dopants. There is a dramatic reduction in the phase transition temperatures of $BiFeO_3$ upon doping determined with differential thermal analyses. This is accompanied by a partial volume of the grains gradually shifting from the bulk rhombohedral towards a higher symmetry one evidenced by X-ray diffraction and Raman Spectroscopy for Sm and Gd doped powders while this effect is minimal in La doped powders. We find that a phase mixture forms in powders whose fraction is a strong function of dopant radius for a given concentration. Moreover, there is a direct correlation between the ionic radius and the extent of reduction in the transition temperature of the polar phase in the mixture for a given dopant concentration. We suggest a mechanism to explain the inhomogeneous nature of the transition of the sol-gel synthesized powders where the dramatic reduction in the transition temperatures of Sm and Gd doped $BiFeO_3$ is due to local lattice strains around unit cells containing dopant ions that create gradients in polarization leading to internal depolarizing fields, possibly stabilizing non-polar phases. We conclude that local disappearance of stereochemical activity of Bi+3 due to lone pairs is not sufficient to explain dramatic changes in phase transition temperatures because of strong dependence on ionic radii of dopants.

A-KONUMUNA GİREN KATKILARIN İYON YARIÇAPLARININ BİZMUT FERRİT'İN FAZ GEÇİŞ SICAKLIĞI VE KRİSTAL YAPISINA ETKİSİ

Mohammadreza Khodabakhsh

Malzeme Bilimi ve Mühendisliği, Yüksek Lisans Tezi, 2013

Tez Danışmanı: Yrd. Doç. İ. Burç Mısırlıoğlu

Keywords:

Ferroic powders, BiFeO3, phase transitions and structure, defects

Özet

Ferroik malzemeler çoğu zaman yeni işlevselliklerin kazanımı veya mevcut özelliklerin iyileştirilmesi amacı ile katkılandırılırlar ancak bunun sonucunda latiste katkı elementlerinin etrafında bölgesel deformasyonlar oluşması kaçınılmazdır. Bu tezde A-konumu katkılandırmasının sol-jel metodu ile sentezlenmiş $Bi_{1-x}A_xFeO_3$ (A: Gd, Sm, La) tozlarının faz geçiş sıcaklıklarına etkisini katkı elementi türü ve miktarına göre değişimini rapor etmekteyiz. Belirli bir katkı oranı için yapı ve geçiş sıcaklıkları arasındaki ilişkinin katkı elementinin iyon yarıçapına net şekilde bağlı olduğunu ortaya koymanın yanısıra elde edilen bulgular katkı iyonları etrafında homojen olmayan latis deformasyonlarının güçlü etkisini ortaya koymuştur. Katkılandırma sonucu $BiFeO_3$ tozlarının geçiş sıcaklığını azalmakta olduğu diferensiyel termal analiz ile tespit edilmiştir ve bu azalma küçük katkı iyonlarının varlığında daha şiddetli olmaktadır. Bu davranışın, Sm ve Gd ile katkılandırılmış tozlarda yapılan XRD ve Raman spektrometresi analizlerinden de anlaşıldığı üzere, tozlardaki bazı tanelerin hacimsel rombohedralden daha yüksek simetriye sahip yapılara geçiş ile eşzamanlı olduğu gözlemlenmiş, La katkılı tozlarda ise minimal seviyede olduğu dikkati çekmiştir. Sonuçlar katkılı tozlarda miktarı güçlü şekilde katkı iyon yarıçapına bağlı faz karışımları oluştuğuna işaret etmektedir. Bunun dışında katkı iyon yarıçapı ile faz karışımının geçiş sıcaklığındaki düşüş şiddeti arasında da doğrudan bir bağıntı gözlemlenmiştir. Çalışmadaki sol-jel tozlarının homojen olmayan faz geçişi davranışını açıklamak için özellikle Sm ve Gd katkılı $BiFeO_3$ tozlarda katkı iyonlarının etrafında oluşan yapısal deformasyonun yol açtığı kutuplaşma farklılıkları ve buna bağlı oluşan iç elektrik alanların etkisini temel alan bir mekanizma öne sürülmüştür. Sonuç olarak faz geçiş sıcaklığının güçlü ve net şekilde katkı iyon yarıçapına bağlı olması, katkı sonucu kaybolmaya yüz tutan Bi+3'teki stereokimyasal aktivitenin gözlemlenen dramatik değişimleri açıklamak için yetersiz olduğunu da göstermektedir.

ACKNOWLEDGEMENTS

First and foremost, I would like to thank my supervisor Dr. Burç Mısırlıoğlu for his support, patience and steadfast encouragement during my experimental work and data analysis. I would also like express my sincere gratitude to him for proof reading my dissertation a number times and providing me with useful suggestions and feedback. This work would not have been possible without the assistance provided by my supervisor, colleagues and friends. They have inspired and motivated me through my studies. A big thank you goes to my parents for their encouragement and support, and for inspiring curiosity from early childhood.

I would also like to thank my reading committee members, Prof.Mehmet Ali Gülgün and Prof. Ali Kosar for the helpful comments during my research and on the draft of this thesis.

This work was supported by TÜBİTAK 1001 Grant 109M686 and partially by funds of TÜBA GEBİP. The authors acknowledge the use of Sabanci University SUNUM facilities for Raman spectroscopy.

TABLE OF CONTENTS

LIST OF TABLES

LIST OF FIGURES

Chapter 1. INTRODUCTION

1.1 Introduction

Multiferroic materials have been on the agenda of many research groups owing to the coexistence of spontaneous electric and magnetic dipoles, namely ferroelectric and magnetic ordering. Many of these compounds actually exhibit improper ferroelectricity as the occurrence of permanent dipoles in these materials is a result of spiral or helical spin structure favoring angled oxygen-cation bonds at low temperatures giving rise to local charge separation that forms the basis of weak but finite amplitude electric dipoles. Such a mechanism of ferroelectricity occurs mostly at temperatures much lower than room temperature (RT) for these materials. $BiFeO_3$ (BFO), as a proper ferroelectric displaying a first order structural transition, has probably been the most interesting compound in this regard because of its very high paraelectric-ferroelectric transition temperature (around 820°C) and Neel point (around 380°C). Such characteristics have allowed proposal of device designs with new functionalities, in particular following the studies claiming that the magnetic ordering and the ferroelectric state are intimately coupled and that domain manipulation both via electric and magnetic fields is possible in thin films. Moreover, reports exist claiming about 10 times increase in the remnant polarization in epitaxial BFO films at RT compared to their bulk counterparts. Despite the continued interest in growth and characterization of BFO thin films, structural and electrical properties of BFO in bulk form have been systematically studied by a few groups. Recent works have mostly focused on the effect of synthesis on morphology and RT phase stability in the presence of dopants in addition to effects of these dopants on polarization and magnetic structures and, very importantly, leakage currents. Many of the hysteresis loops in the works cited above have tendencies to fatten, a major sign of leakage. Leakage has been a foremost problem in BFO films and powders. While domain walls have been held responsible for leakage many of the above citations attribute leakage to the volatility of the Bi+3 ions that, when these sites are vacant, they act as *p*-type centers, accepting electrons from the valence band and causing *p*-type conduction both in films and bulk form. Bi+3 ion vacancies have also been

held responsible for oxygen vacancy formation to sustain local electrostatic neutrality, which can again result in increased conductivity. Owing to the fact that a few A-site compatible ions such as La, Sm, Gd, Pr and Nd have significantly higher bond enthalpies with oxygen than the Bi-O bond, they are often added to BFO in order to minimize carrier donating/trapping vacant sites via stabilizing the oxygen in the lattice in addition to rendering a more "useful" magnetic structure for potential applications especially in the case of Gd and Sm. From the point of view of leakage, compensation of vacancy generated carriers via doping can lead to a more "intrinsic" BFO with relatively less free carrier densities. Rare earth elements compatible with Bi+3 ions in radius that can substitute the A-sites stabilize Bi and oxygen along with reduction of the concentration of *p*-type centers accompanied by a shift of the Fermi level towards the middle of the band gap, which is one way to reduce and control the leakage currents as shown in our recent work. Apparent polarization enhancement has also been attributed to the reduced leakage via La substitution to Bi sites, reducing the available Fe 3d states that would otherwise drive a hopping-type conduction mechanism. A-site doping has also shown that the formation of secondary conducting phases can be prevented, likely upon stabilization of oxygen via higher bond enthalpy of dopants helping to sustain the equilibrium stoichiometry. On the other hand it is well understood that doping the BFO with A-site substitutes should be expected to change the transition temperatures and impact the ferroelectric properties at RT as with any other polar oxide. However, we came across only a few articles that analyze the effect of various dopants on phase transition temperatures and characteristics. There have been numerous reports on the ferroelectric and magnetic properties of BFO mostly at RT as a function of dopant type and concentration only some of which we can cite here. A significant number of these studies are dedicated to thin films where misfit strains induced by the substrate are expected to screen structural impact of dopants and make the study of their effect alone rather difficult. Moreover, that the film structure tries to cope with the misfit strains via several elastic variants of "strain stabilized" crystalline structures carry the discussion on dopant effects to an entirely different setting. Generally speaking, that the ferroelectric properties can diminish with dopants is often discussed envisioning unitcells shifting to higher symmetry upon doping. Dopant effects in BFO have almost always considered from the point of view of the local stereochemistry of bonding of bismuth with

oxygen however this mechanism solely on its own cannot explain the significant reduction in the phase transition temperatures that strongly depend on ionic radius mismatch with Bi+3 and additional mechanisms at a more global scale need to be considered. Dopants also create extended inhomogeneous strain fields in the lattice. Strain effects in BFO are quite well understood in thin film studies where the stabilized phases can be identified for a given misfit with the substrate and a similar approach can be employed to evaluate dopant effects in powders. With this in mind, we carried out a structural study to probe the effect of RE A-site dopant radius on the structure of $BiFeO_3$ combined with a DTA analysis to determine the Curie point of this material and propose a mechanism to qualitatively but consistently explain the the dopant radius sensitivity of BFO. Here, we report on the structural changes of sol-gel prepared high quality BFO powders upon doping with La, Sm and Gd respectively. These dopants have a range of ionic radius misfit with Bi with La being the closest to Bi and Gd having the largest misfit. XRD studies along with Rietveld refinement is carried out followed by Differential Thermal Analysis (DTA) and Micro Raman Spectroscopy. Scanning Electron Microscopy was carried out to characterize the grains size and morphologies of our powders with the intention of understanding whether we might be encountering size effects in doped powders, i. e. disappearance of the ferroelectric state due to small grain size. One way to check this is to carry out hystereses measurements on compacted powder samples. Noting that bulk BFO in powder form, despite its very high Curie temperature, has a small remnant polarization (around 3 μC/cm2) compared to materials like $BaTiO_3$ or PZT, moderate amounts of leakage in the presence dopants can easily overwhelm the displacement currents emanating from dipole switching during hysteresis measurements, rendering detection of ferroelectricity nearly impossible. To probe the existence of the polar phase in our powders, we chose to conduct Raman spectroscopy as we failed to obtain any reasonable hysteresis or butterfly-type capacitance-voltage curves due to unacceptable amounts of leakage in our samples. We found a direct correlation between the changes in structural characteristics of BFO upon doping with the reduction in Curie temperatures as a strong function of dopant radius. Finally we propose a mechanism to qualitatively but consistently address the complicated and dopant radius dependent behavior of the phase transitions we observe in DTA experiments based on the magnitude of the lattice strain the dopants induce.

1.2 Ferroelectricity

Ferroelectric materials can be considered as dielectrics which have a switchable spontaneous electric polarization (P_S) in absence of an external electric field. The direction of the polarization can be switched by an oppositely aligned external electric field larger than the coercive field (E_C). One classic signature of ferroelectricity is the polarization-electric field hysteresis loop. In linear dielectric materials the polarization is proportional to the applied field, but for ferroelectric materials the polarization has an additional hysteretic component. This non-linear behavior of polarization (P) as a function of electric field is shown in Figure 1-1. The ferroelectric polarization and coercive fields can be determined from a hysteresis loop. Polarization will saturate at sufficiently large fields, and a remnant polarization (P_r), or spontaneous polarization, prevails in zero electric field. Ferroelectric materials undergo a structural phase transition from a paraelectric phase to a ferroelectric phase upon cooling through the Curie temperature (T_C).

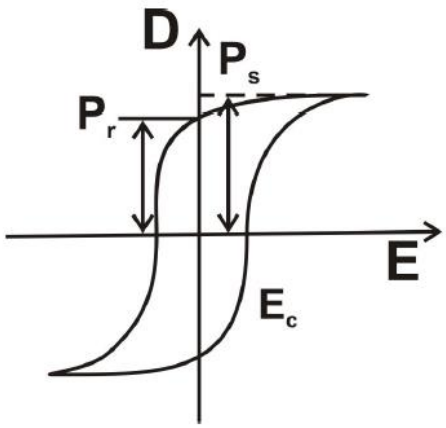

Figure 1-1. Hysteresis loops characteristic for the ferroic properties of ferroelectricity

The dielectric constant ε which is a measure of the polarisability of the material is large in ferroelectric materials, and diverges at the Curie temperature, when the polarization is most susceptible to applied electric fields. The symmetry of the crystallographic point groups imposes restrictions on the possibility of ferroelectricity in a crystal. There are 32 crystallographic point groups out of which 21 are non-centrosymmetric. Twenty of these

21 point groups exhibit piezoelectricity in which mechanical stress can induce polarization, and vice versa: an electric field can induce strain. Piezoelectricity is a strong, linear coupling between electric polarization and mechanical stress, opposed to the weak, quadratic electrostriction effect found in all dielectric materials. Ten of the twenty non-centrosymmetric point groups possess one unique polar axis and hence exhibit pyroelectricity in which a change of temperature will induce a change of polarization. All pyroelectric materials are also piezoelectric, but piezoelectric materials without one unique polar axis are not pyroelectric. All ferroelectric materials are pyroelectric, but not all pyroelectrics are ferroelectric. The unique characteristic is whether the spontaneous polarization can be switched by an external field or not, a feature which must be tested experimentally as it cannot be predicted a priori from symmetry considerations.

Depending on the origin of the polarization, we can classify Ferroelectric materials into proper or improper, and the difference lies in the mechanism by which (the primary order parameter) ferroelectricity occurs. For instance, $BiFeO_3$ is a proper ferroelectric because the origin of the ferroelectric behavior is ionic displacements owing to a structural transition. Many other magnetoelectric materials, on the other hand such as $YMnO_3$ are improper ferroelectrics because the permanent dipoles arise as a result of a cycloidal spin ordering that favors of slight shifts of oxygen-Mn bonds leading to asymmetric charge distribution, hence dipoles. Above T_C, the crystal has a centrosymmetric structure and has no spontaneous polarization. Below T_C, the crystal exhibits ferroelectricity and has a structure resulting from a change in the symmetry of the unit cell. As a perovskite ferroelectric is cooled below T_C, the central ion in the unit cell displaces from its equilibrium position to create a spontaneous polarization. In displacive ferroelectrics the spontaneous polarization arises from displacements of cations with respect to the anion sublattice, creating electric dipoles which are aligned in one direction, breaking the inversion symmetry. In contrast with conventional displacive ferroelectrics, also known as proper ferroelectrics, polarization in improper ferroelectrics is not the primary order parameter. In improper ferroelectrics polarization results as a secondary effect from a lattice distortion, e.g. in magnetic spin spiral induced ferroelectrics. Polarization can also arise from ordering of the orientation of anion groups, charge ordering (electronic

ferroelectrics) [1], orbital ordering [2], cooperative tilting of polyhedra (geometric ferroelectrics) [3], or layered ordering in asymmetric super lattices [4]. Long range Coulombic forces are responsible for the alignment of electric dipoles in one direction in

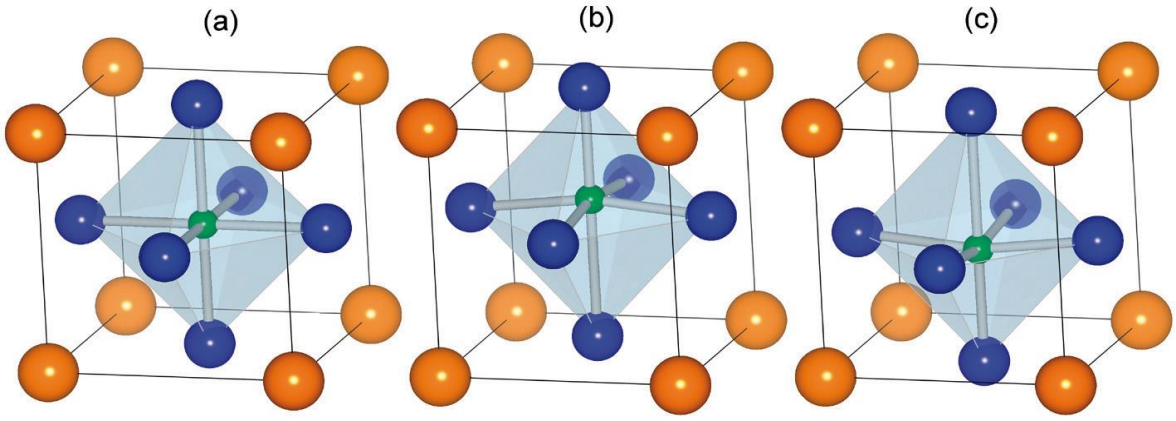

Figure 1-2. Unit cells of paraelectric cubic (a) and ferroelectric tetragonal perovskite with polarisation up (b) and down (c). A cations(orange), B cations(green) and oxygen anions (Blue) are situated in the corners, centres and faces of the unit cells, respectively.

displacive ferroelectrics, while short range Coulombic forces (e.g. ionic bonds) support centrosymmetry; ferroelectricity thus requires long-range forces to dominate over short range forces. Partial covalent bonding is the common mechanism for stabilizing ferroelectric dipoles by off-centering of cations relative to the anion sublattice. We have three principal types of perovskite oxides based on cation valence distribution; I-V, II-IV and III-III perovskites. The simple, cubic perovskite structure is shown in Figure 1-2. the larger A cation resides in a 12-coordinated dodecahedron, while the smaller B cation is octahedrally coordinated. In the prototype ferroelectrics $BaTiO_3$ and $PbTiO_3$ the centrosymmetric, high temperature cubic structure transforms to a tetragonal, polar structure below the Curie temperatures of 123° and 490°C, respectively. The cation is displaced towards an apical oxygen along the long c-axis of the tetragonal unit cell, breaking inversion symmetry and providing electric dipoles along the [001] direction. Partial covalent bonding between empty d orbitals of Ti^{4+} and O 2p orbitals stabilizes the

off-centering atom relative to the inversion symmetry centre of the TiO6 octahedron, as shown by first principles calculations and verified experimentally [5]. The substantially higher T_C, tetragonality (unit cell distortion c/a) and spontaneous polarization of $BaTiO_3$ and $PbTiO_3$ shows the importance of the 6s2 lone pair of Pb^{2+}, as it takes part in partial covalent bonding with O 2p orbitals. Partial covalent bonding between O 2p and 4d orbitals of Nb^{5+} have also been identified in $KNbO_3$ [6], thus partial covalent bonding is not restricted to the titanate perovskites. In general, the extent of covalency between A and O sites in ferroelectric crystals is understood to impact the Curie temperature and polar stability.

1.3 Multifunctional materials

Multifunctional materials are in demand for new generation technologies and prime candidates for high-density computer memory concepts, as well as for sensors and spintronics devices. In the development toward device miniaturization and high-density data storage system, it becomes highly desirable to integrate multifunction in a single material. They combine two or more of the ferroic properties ferromagnetism, ferroelectricity (chapter 1-5) and ferroelasticity. Perovskite materials have generated much interest in recent years. They are compatible with Si and SiO_2, the two materials the information technology industry is based on, and thus one of the most promising classes of materials for technological applications, particularly due to their magnetic and electric properties. More interesting is that these ferroelectric and antiferromagnetic properties are present at room temperature [7]. Such materials seem to be promising candidates for spintronics and magnetoelectronics. $BiFeO_3$ (BFO) is one such material that has received much attention and it is perhaps the only material that is both magnetic and a strong ferroelectric at room temperature, in the same phase and spontaneously. One of the most important requirements for magnetoelectric multiferroics predicted by P.Curie [8] on the basis of symmetry considerations. The primary conditions for ferroelectricity are the non-centrosymmetric structure, which allows the dipole formation and spontaneous polarization. There are 31 (out of 122) Shubnikov Heesch point groups that allow

spontaneous electric polarization and 31 that allow spontaneous magnetization. There is only 13 Shubnikov points, which allow both spontaneous magnetization and spontaneous electric polarization in same phase. The symmetry considerations itself restrict the number of multiferroics. We can divide magnetoelectric multiferroics into two types. First type of multiferroics contains those perovskites in which ferroelectricity and ferromagnetism have different origins (cations at A-site and B-site respectively). These materials show weak magnetoelectric coupling. In these materials, ferroelectricity typically appears at higher temperatures than magnetism and they exhibit large spontaneous polarization just like $BiFeO_3$. These materials have been extensively studied since 1960's. However, major challenge in these materials is to enhance the values of magnetoelectric coupling coefficient. These multiferroics are further classified in many subclasses on the basis of origin of ferroelectricity which are: I) Ferroelectricity due to shifting of B-cation, II) Ferroelectricity due to lone pairs, III) Ferroelectricity due to charge ordering and IV) Geometric ferroelectricity. Most of Bismuth (Bi) and Lead (Pb) based perovskites show ferroelectricity due to lone pair, for example $BiFeO_3$, $BiMnO_3$, and $PbVO_3$. In these materials Bi^{3+} and Pb^{2+} have two outer 6s electrons that do not participate in chemical bonds. These electrons are called "lone pairs" or sometimes dangling bonds. Microscopically, one can explain the origin of ferroelectricity in these compounds by the ordering of these lone pairs (with certain admixture of p-orbitals) in the direction of electric field. The magnetism in these materials is originated from B-cation. The second type is Magnetic Multiferroics in which the ferroelectricity is originated from magnetism and implies strong magnetoelectric coupling.

1.4 Cubic oxide perovskite materials

The cubic perovskite structure has the general stoichiometry ABO_3. The traditional view of the cubic perovskite oxide lattice is that it consists of small B cations within oxygen octahedra, and larger A cations which are XII fold coordinated by oxygen. For the some oxides like $BiFeO_3$ or $LaAlO_3$ with $A^{+3}B^{+3}O_3$ perovskites structure, the most symmetric structure observed is rhombohedral R3c which involves a rotation of the BO6 octahedra

with respect to the cubic structure However, this distortion from the perfect cubic symmetry is slight. The structure of an ideal cubic perovskite is shown in Figure 1-1, where the A cations are shown at the corners of the cube, and the B cation in the centre with oxygen ions in the face-centred positions. The space group for cubic perovskites is Pm3m. Literature suggests that many of the materials exhibit the orthorhombic Pnma (or Pbnm) distorted structure at room temperature. A further distortion is also possible resulting in a rhombohedral structure with the space group R3c. The rhombohedral structure is shown in Figure 1-4. However, with decreasing A cation size, a point will be reached where the cations will be too small to remain in contact with the anions in the cubic structure. Therefore the B-O-B links bend slightly, tilting the BO6 octahedra to bring some anions into contact with the A cations. To allow for this distortion, a constant, t, is introduced into the equation 1.1.

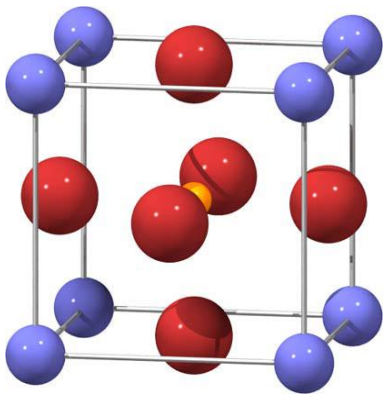

Figure 1-3 Cubic perovskite unit cell. Blue spheres represent the A cations, yellow spheres represent the B cations, and red spheres represent oxygen anions forming an octahedra.

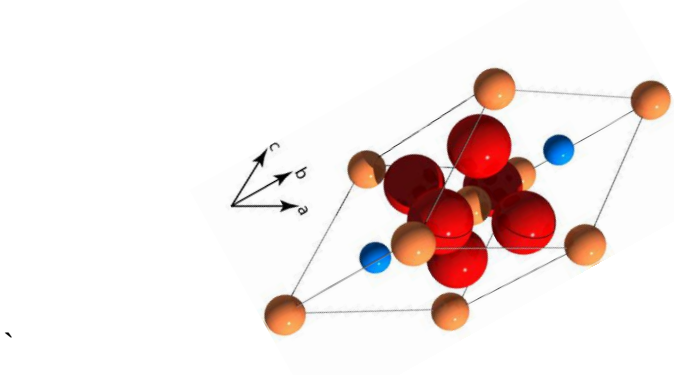

Figure 1-4 R3C rhombohedral perovskite unit

The constant, *t*, is known as the tolerance factor and can be used as a measure of the degree of distortion of a cubic perovskite structure from ideal cubic (Figure 1-5). Therefore, the closer to cubic, the closer the value of the tolerance factor is to unity. All perovskite distortions that maintain the A and B site oxygen coordinations involve the tilting of the BO6 octahedra and an associated displacement of the A cation. For the orthorhombic structure, these octahedra tilt about the b and c axis, while in the rhombohedral structure the octahedra tilt about each axis. This octahedral tilting is related to the sizes of the A and B cations (as described by the tolerance factor).

$$R_A + R_O = t\sqrt{2}(R_B + R_O) \qquad (1\text{-}1)$$

Perovskite materials are fascinating because they display a wide variety of fundamental properties, from magnetism to ferroelectricity, from colossal magneto-resistance to half-metallicity [9]. These materials are used in a number of important technological applications such as electromagnets, sensors and optical storage devices. In recent years multi-ferroic materials have attracted significant interest as they exhibit ferroelectric and ferromagnetic properties. In particular, after the discovery of large electric and magnetic polarization effects in thin BFO films [7], much attention has been devoted to the properties of $BiFeO_3$. ABO_3 oxide perovskites which are rhombohedral at low temperatures, such as $BiFeO_3$, $LaAlO_3$, $PrAlO_3$ or $NdAlO_3$ have ferroelastic instabilities at

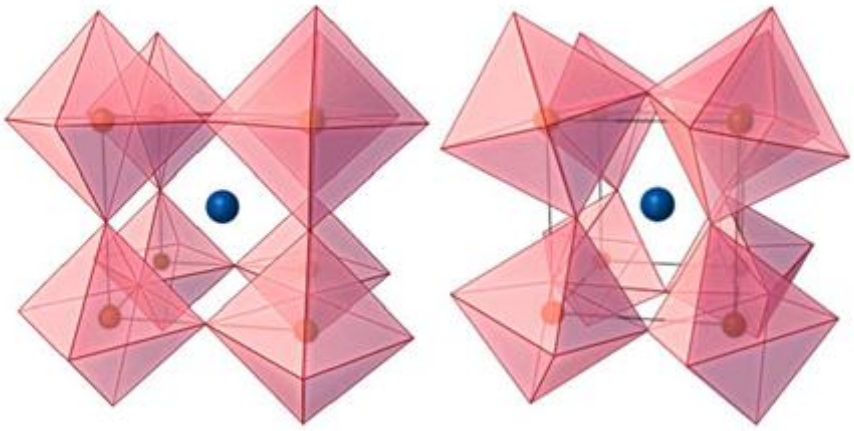

Figure 1-5. Perovskite distortion from (left) cubic to (right) orthorhombic

the A-ion site that induce displacive phase transitions directly to cubic, but those which have B-site instabilities instead have order-disorder transitions to cubic that involve two or more steps. The quest to understand room temperature ferroelectricity of BFO has led to an advent of research in this area [10] and its possible applications. More interestingly is the possible existence of both electronic and magnetic properties in such a material, with miniaturization opening the possibility of combining [11] both these properties into a multi-functional material to produce a single device component to perform one task. Such materials are rare in nature as the conditions of being simultaneously ferroelectric (materials with a spontaneous electric polarization that can be switched on by an applied electric field) and ferromagnetic (empty and partially filled transition metal orbits) cannot exist at the same time [12].

1.5 Bismuth Ferrite

Bismuth ferrite also commonly referred to as BFO is an inorganic chemical compound with a perovskite-type structure. The structure of bulk $BiFeO_3$ is usually described in three different geometrical ways. The most accurate description is that $BiFeO_3$ is rhombohedral at room temperature with the space group R3C . This is equivalent to the hexagonal setting often used by crystallographers, which has six formula units of $BiFeO_3$ in the hexagonal cell and lattice constants of a_{hex} =5.579 Å and c_{hex} = 13.869 Å. Bismuth ferrite is an example of perovskite structure that attracts attention not only because of its ferroelectric properties but also because of its magnetic ordering coupled with its ferroelectric behavior. It shows a high temperature paraelectric-ferroelectric phase transition (Curie temperature of 1083K, and Néel temperature of 657K) , which means that $BiFeO_3$ is a stable ferroelectric in room temperature showing magnetic behavior in the meantime. The idea of using multiferroics in applications for multifunctional device components arouses interest on materials in which the magneto-electric property is tailored. In these materials polarization and magnetization can be weakly or strongly coupled [13], Due to coexistence of antiferromagnetism and ferroelectricity (magneto-electric effect) the net magnetization would be changed by applying an electric field, or the polarization increased by applying a magnetic field. Although the linear magneto-electric effect is theoretically forbidden by the symmetry of bulk $BiFeO_3$ [14], a linear effect in $BiFeO_3$ films has been reported [15]. It should be noted a certain class of materials, prominently oxides exhibit the presence of a magnetic structure along with ferroelectricity in the same phase [16].

The nature of the ferroelectric transition of $BiFeO_3$ and its paraelectric structure has thus not yet conclusively been identified, although cubic Pm3m, rhombohedral R3m, orthorhombic P2mm, and tetragonal I4/mcm and monoclinit have been suggested [17,18,19,20,21]. $BiFeO_3$ exhibits spontaneous polarization along the [100] direction. However, a serious problem with $BiFeO_3$ that has greatly limited its applications is that it has very high values of leakage current. This high amount of leakage current is mainly attributed to deviation from oxygen stoichiometry and high defects density [22]. There are charge defects present in the system such as bismuth vacancies (V_{Bi}) and oxygen vacancies (V_o). Creation of V_o is a result of Bi volatility and the transition from Fe^{3+} to Fe^{2+}.

Equations 1.2 and 1.3 suggests that charged defects governed by ions, oxygen vacancies V_o and/or bismuth vacancies V_{Bi} may appear in both the deoxygenated $BiFeO_3$ phases and deoxygenated impurity phases. These V_o and/or V_{Bi} vacancies will reduce the electrical resistivity of the samples, giving rise to high leakage currents in the samples [22]. In this situation, theoretical prediction of observing multiferroic behavior turns into high conductivity due to valence fluctuation between Fe^{3+} and Fe^{2+} ions and oxygen deficiency in the system.

$$2Bi^{2+} + 3O^{2-} \rightarrow Bi_2O_3 + 3V_o^{2+} + 2V_{Bi}^{3-} \qquad (1.2)$$

$$2Fe^{3+} + O^{2-} \rightarrow 2Fe^{2+} + 0.5O_2 + V_o^{2+} \qquad (1.3)$$

Below the Curie temperature, the cubic lattice will be tetragonally distorted which is a displacive ferroelectric phase transition. As mentioned before, bismuth ferrite exhibits a rhombohedral ferroelectric phase. As in Figure 1-2 local atomic arrangement in perovskite structure can acquire a position so that there will be some remnant polarization after applying sufficient electric field. In this situation unit cells contain a permanent electric dipole.

Variety of atoms occupying A-site and B-site positions in oxide perovskites create different mechanisms of ferroelectricity and various levels of magnetic substructure. In $BaTiO_3$ for instance, ferroelectricity occurs due to the asymmetric shift of Ti while the lone-pair Pb ion is dominant in $PbTiO_3$ [23] again accompanied by Ti shifts in the unitcell. In our study with $BiFeO_3$, the later one is the case where the polarization is mostly caused by the lone pair of Bi^{+3}, meaning the A-site positions involvement while the magnetization comes from the B-site (Fe^{+3}).

1.6 Applications of $BiFeO_3$

$BiFeO_3$ is a prime candidate for magnetoelectric memories, where bits can be written by an electric field, utilizing the ferroelectric polarization, and read from the associated magnetic field, avoiding destructive read-out of the ferroelectric state. Reading antiferromagnetic states is not straightforward, and an obvious solution to this is to read the magnetism of a ferromagnetic layer in contact with antiferromagnetic $BiFeO_3$, exploiting the associated exchange bias [24]. Exchange bias offsets and/or widens the magnetic hysteresis loops, and exchange bias between $BiFeO_3$ and several ferromagnetic materials has been reported. Voltage control of an exchange biased ferromagnetic layer has been demonstrated [25]. A possible Magnetoelectric Random Access Memory (MERAM) element using $BiFeO_3$ is shown in Figure 1-6 . A voltage V controls the ferroelectric state of $BiFeO_3$, and given the strong coupling between the antiferromagnetic plane and ferroelectric polarization, switching the ferroelectric polarization by 71 or 109 ° can change the antiferromagnetic planes, and thereby flip the direction of the lower ferromagnetic (FM, blue) layer through exchange bias if the coupling is strong enough. In the FM-Metal-FM trilayer the alignment of the FM layers can thus be controlled to be parallel or antiparallel by the ferroelectric state of the green $BiFeO_3$ layer.

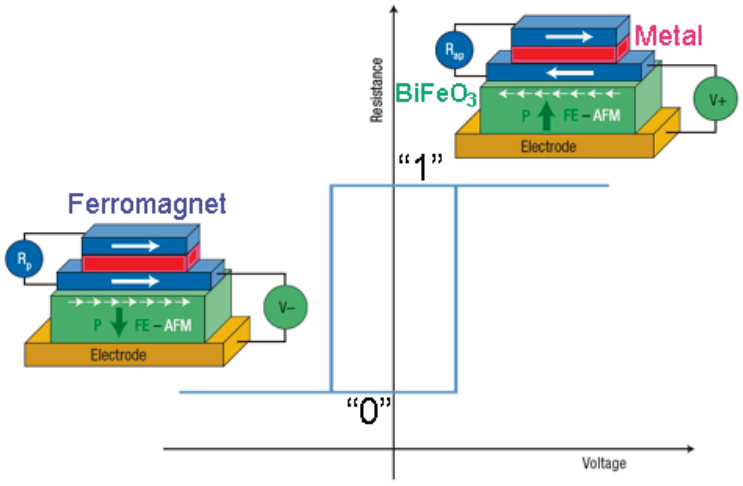

Figure 1-6. A concept for a MERAM element utilizing BiFeO3 (green FE-AFM layer, ferroelectric antiferromagnet).

Parallel FM layers give a lower resistance across the FM-Metal-FM trilayer, corresponding to the binary state "0". Oppositely, antiparallel alignment of the FM layers give a higher resistance, corresponding to the binary state "1", as in conventional read-out of bits utilizing Giant Magnetoresistance. $BiFeO_3$ can also be used as a tunneling barrier layer as it is ferroelectric down to 2 nm thickness [26]. The ferroelectric state can control the direction of magnetisation in adjacent ferromagnetic layers, and thus the tunneling magnetoresistance [27]. The direction of the polarization can also directly control the tunneling resistance, enabling non-destructive read-out of ferroelectric bits.

As $BiFeO_3$ is a lead-free, non-toxic ferroelectric with the highest switchable polarization known among perovskites, it is a primary candidate for substituting $PbZr_{1-x}Ti_xO_3$ (PZT). It is possible to incorporate into Si and SiO_2 based circuitry, and can thus be used for FeRAM, which do not utilize the magnetic properties. Leakage currents must be controlled and minimized to utilize the ferroelectric polarization, regardless of whether the magnetism is active as in MERAM or "passive" as in FeRAM concepts. Chemical compatibility, fatigue and voltage stressing are other challenges for $BiFeO_3$-based ferroelectric memories [28]. Pure $BiFeO_3$ has a too low piezoelectric coefficient to challenge PZT, but pulsed laser deposition (PLD) grown films of $Bi_{1-x}Sm_xFeO_3$ an exhibit a piezoelectric coefficient d33 of > 100 pm/V at a morphotropic phase boundary, and are promising candidates for lead-free piezoelectrics [29]. Emission of tetrahertz radiation from $BiFeO_3$ when illuminated with a femtosecond laser pulse is correlated with the ferroelectric state. THz emission has thus the potential of being a non-destructive and very fast way of reading ferroelectric bits. It has the further advantage that it is insensitive to leakage currents.

1.7 Size effect on the ferroelectric phase transition

The great fascination of nanostructure materials is that their properties are different from, and often superior to, those of conventional materials that have phase or grain structures on a coarse size scale. On the other hand, phase stability is an important aspect of materials

with reduced spatial dimensions in the nanometer size scales. The reduction in physical sizes of ferroelectrics from the macroscopic down to the mesoscopic system usually gives rise to a change in stability of the polarization [30,31]. Experimentally it is well known that the physical properties can be inhibited [31] or even enhanced [30] in nano-structured materials, i.e., zero-dimensionality (O-D) atom clusters and cluster assemblies, or thin films. The polarization on the other hand usually suffers a degradation in nanosize ferroelectric films or clusters due to the fact that the surface usually behaves much different than bulk. Finite size effects and their induced abnormalities in ferroelectrics can be explained by four different circumstances:

- Mono-domain configuration: many size effects in ferroelectrics are explained by the occurrence of a mono-domain configuration, which is energetically favorable in systems with small size. However, this effect is unrelated to a change in the structural instability of a polar phase as the physical dimensions or sizes are reduced.

- Depolarizing field effect: Quite a number of size effects in ferroelectric systems can be attributed to a depolarizing field effect [32]. In a mono domain system, if the surface bound charges are not compensated, strong depolarizing fields can suppress ferroelectricity. Nevertheless, not only the depolarizing field effect seems to be much weaker than expected , but also it cannot explain why sometimes ferroelectric stability can be even enhanced in some types of thin films or nanometer-sized materials [30].

- Surface effect: it is third source of strong finite size effects on polarization stability [30] or more generally, an interface effect. There are two main physical consequences of surface effects. (1) Close to the surface of a system the original translational invariance of the system tends to be broken as compared to the bulk interior. As a result, changes in the local symmetry and features of soft modes occur such that the polarization characteristic (dipole-dipole interactions) at the surface differs from that within the interior [33]. Accordingly, the total energy of the system

is altered by the surface effect, which is represented by a sulfate energy or a surface tension and is proportional to the total surface area. (2) As the physical sizes of a confined system reach a mesoscopic level (100 nm or less), the fraction of atoms located in (or near) surfaces increases substantially. They are structurally associated with surface or interfacial environments, thus surface effects can play a vital role in controlling the properties of nanostructure materials.

- Defects can have a very strong influence on the physical properties of ferroelectric structures especially in confined geometries such as sub micron powders and thin films. The study of dopants effects in the current thesis is also an example to demonstrate the impact of "introduced" point defects via dopants to A-sites whereby it will be shown in the rest of the thesis that the "strength" of the defect (which, here means how strongly the defect distorts or alters the regular ferroelectric lattice) can become a prominent factor even when the defect concentration is relatively low (a few percent).

Chapter 2. EXPERIMENTAL

2.1 $BiFeO_3$ Synthesis

In order to synthesis the $BiFeO_3$, several techniques have been used to overcome its leakage problem. Solid-state reaction [34], co-precipitation method [35] and soft chemical route [36] are some methods that have been used to synthesis $BiFeO_3$ with minimum leakage current. On the other hand, it is crucial to introduce a well-defined fabrication procedure of synthesizing pure single phase $BiFeO_3$. Bismuth ferrite is very prone to show parasitic phases that tend to nucleate at grain boundaries and impurities [37] and as it is shown in compositional phase diagram of $BiFeO_3$ (Figure 2-1) [19] According to the phase diagram, $BiFeO_3$ is a stable compound up to the peritectic decomposition temperature of 930-934 °C, where $BiFeO_3$ melts incongruently. In contrast with the phase diagram, which shows the equilibrium thermodynamic properties, $BiFeO_3$ has frequently been claimed to be metastable at high temperatures, above 750-830. The pseudo-binary phase diagram of the system $Bi_2O_3 - Fe_2O_3$ contains three ternary phases at room temperature; $BiFeO_3$ with perovskite structure, $Bi_{25}FeO_{39}$ and $Bi_2Fe_4O_9$ with sillenite and mullite composition respectively. The formation of the sillenite and mullite phases is a challenge during ceramic and chemical synthesis routes to obtain $BiFeO_3$. Any slight change in procedure parameters could lead to forming other impurity phases present in Bi-Fe-O system, such as Bi or Fe rich phases, like $Bi_{25}FeO_{39}$, $Bi_2Fe_4O_9$, $Bi_{24}Fe_2O_{29}$ and unreacted Bi_2O_3 [38,39]. Impurities and oxygen vacancies are also important for thin films, because they are known to artificially enhance the remnant magnetization. Minimizing them requires very careful modification of growth parameters.

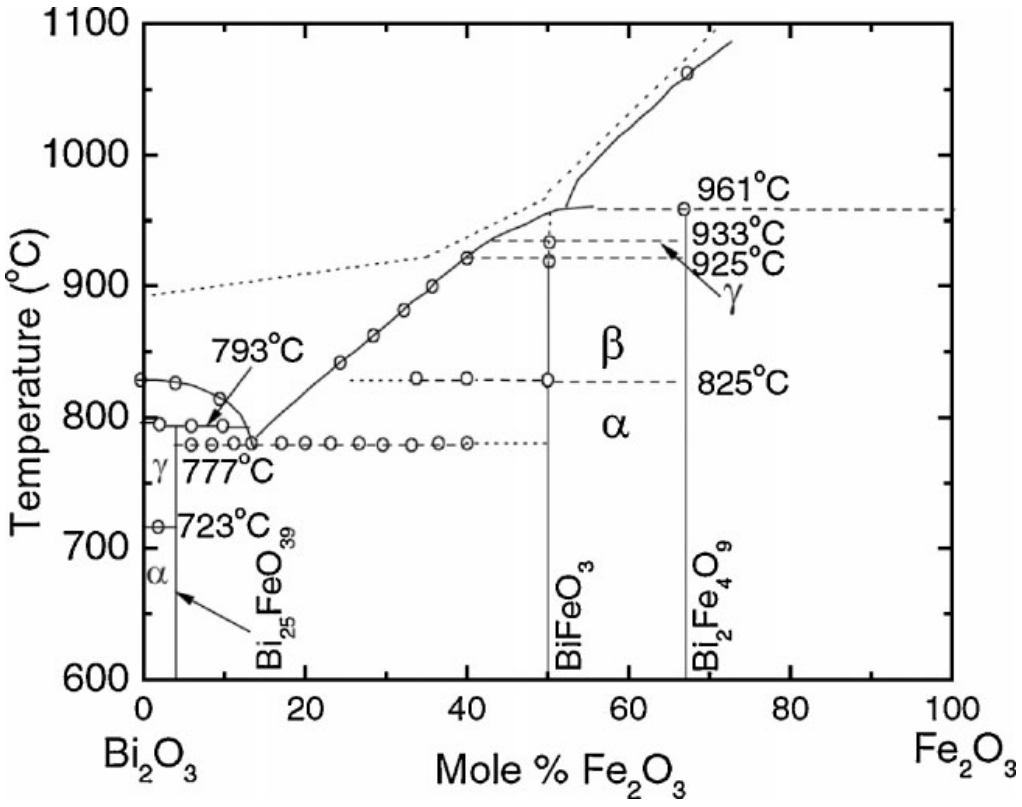

Figure 2-1 Phase diagram of the Bi_2O_3 – Fe_2O_3 system [19]

There are several significant advantages of sol-gel method which we used in comparison to other methods like solid-state calcination. First of all it is energy efficient and cost effective because it is relatively low temperature process and easy to control the stoichiometry of the system. Other advantages are association of solid colloidal state with liquid medium, thus avoiding any pollution by the eventual dispersion of dust. We can also control the kinetics of the various chemical reactions by the low processing temperatures and by the often dilute conditions. The nucleation and growth of the primary colloidal particles can also be controlled in order to give particles with a given shapes, size and size distribution. Finally it allows us to obtain materials with high purity and homogeneity which are not possible to be produced by solid-state fusion can be produced by this method and unlike the solid state reaction it doesn't need addition purification step like leaching in acids. Better stoichiometric control and avoiding contaminations. Flowchart given in Figure 2-2 is an outline of the sol-gel method we used for the synthesis procedure. Bismuth nitrate pentahydrate [$Bi(NO_3)_3.5H_2O$] and iron nitrate nonahydrate [$Fe(NO_3)_3.9H_2O$] (99.99% Sigma-Aldrich) were used as Bi and Fe based chemicals respectively. By dissolving Bi and

Fe nitrates in ethylene glycol and acetic acid separately followed by mixing at room temperature, we obtained a transparent precursor solution. This precursor solution was used both in powder synthesis and in spin coating to fabricate near-epitaxial films. It should be mentioned here that we don't discuss the results from thin film preparation and electrical properties investigate of $BiFeO_3$ in this thesis but focus on a structural characterization route to shed light on structural effects of A-site dopants with various ionic radii.

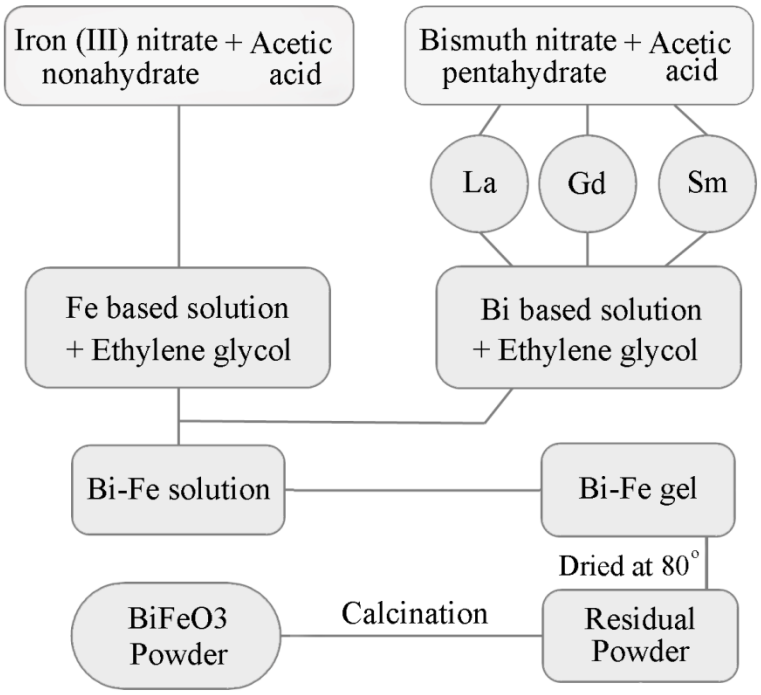

Figure 2-2 Flowchart of the synthesis process for obtaining pure and doped $BiFeO_3$ powders

To investigate the effect of A-site doping, Gd, La and Sm elements were added in different doping levels (1, 5, 10 and 15%). For Gd doping, gadolinium nitrate hexahydrate $[Gd(NO_3)_3.6H_2O]$, for La, lanthanum nitrate hexahydrate $[La(NO_3)_3.6H_2O]$ and for Sm, samarium nitrate hexahydratewere $[Sm(NO_3)_3.6H_2O]$ all 99.99% from GFS chemicals substituted to same percentage of bismuth nitrate pentahydrate in the first stage. A two-stage thermal path was used for calcination where the precursor solutions were kept in

550°C and 700°C each for 1 hour and the heating rate was 10°C/min. Then powders were free-cooled down to room temperature to get $BiFeO_3$ phase (Figure 2-3). In previous studies on $BiFeO_3$, the purity of the phase is mostly reported to be related to the temperature, atmosphere and time at the calcination stage as well as the type and amount of doping elements [36]. Our findings suggest that a combination of drying stage and calcination path is the most important part of the synthesis. It is crucially important to dry the solution in a particular temperature to prevent obtaining precocious gel. In Gd doping for instance, single phase $BiFeO_3$ can form in different heat treatment paths during calcination for different Gd doping levels when the drying stage is done properly as long as the gel is not precocious.

After calcination step, X-ray diffraction (XRD), Differential Thermal Analysis (DTA) and Raman Spectroscopy were used for characterization of powders. The chemical or physical changes which are not accompanied by the change in mass on heating are not indicated in thermogravimetric but there is a possibility that such changes may be indicated in DTA. In DTA technique, the heat changes within a material are monitored by measuring the difference in temperature (ΔT) between the sample and the inert reference. This differential temperature is then plotted against temperature or time to get DTA curve. $BiFeO_3$ has high Curie temperature (T_c830 ºC), high Neel temperature (T_N370 ºC), What is important here is that such a reduction in lattice parameters with increasing Sm, Gd and La content should be expected to impact the T_c. To do so we carried out TG/DTA experiments with cooling and heating cycles at the rate of 10°C/min. To make sure that the temperature at the value of 900º C will not affect the synthesized $BiFeO_3$ in terms of forming new phases that might change DTA results, the stability of the obtained $BiFeO_3$ was checked at high temperatures. To do so, crystallized $BiFeO_3$ powder was heated up with the same regime exerted in the TG/DTA to the samples. The structure of the sample was checked after this heat treatment through XRD analysis. XRD results confirm that there is no extra chemical phase formation during the DTA/TG test.

Raman scattering has proven to be a valuable technique to obtain information about local structures within materials. Since Raman scattering spectra are sensitive to atomic

displacements, the evolvement of Raman normal modes with increasing dopant content can provide valuable information about ionic substitution and electric polarization. The presence of Raman active modes can be used to evaluate the structural order degree at short-range and vibrational modes of the powder obtained in the hydrothermal microwave tend to disappear which can be related to structural disordering at short range, as well as a phase transition for an ordering crystal structure. Therefore, small changes observed in the spectra can be associated with the preparation method, average crystallite size and the degree of structural order. It is known that $BiFeO_3$ belongs to distorted rhombohedral structure with R3c space group. 10 atoms in the unit cell of this structure yields 18 optical phonon modes $\boldsymbol{\Gamma}_{opt} = 4A_1 + 5A2 + 9E$. According to group theory $\boldsymbol{\Gamma}_{Raman} = 4A_1 + 9E$ are 13 Raman active modes, whereas $5A_2$ are Raman inactive modes. The A_1 modes are associated with Fe ions and E modes are associated with Bi ions. More details about raman spectra of the $BiFeO_3$ sample are discussed and illustrated in next chapter.

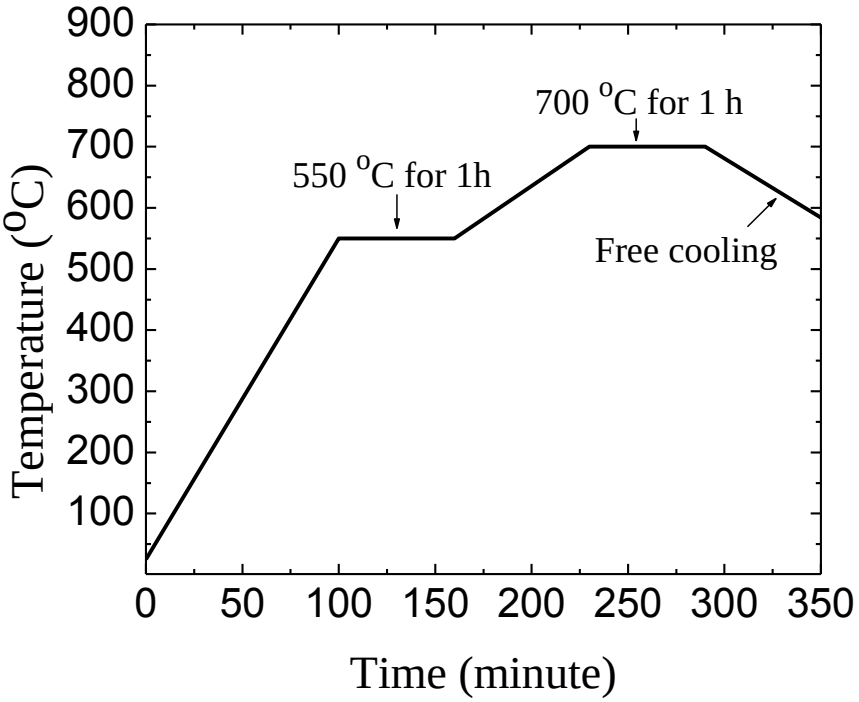

Figure 2-3. The heating and cooling regime during crystallization followed to get pure and doped powders

Chapter 3. RESULTS AND DISCUSSION

3.1 X-ray diffraction Results and Rietveld Refinement

The crystalinity and structure of the powders calcined at various doping levels was characterized by an X-ray diffractometer (BRUKER axs XRD) with Cu K radiation and data were collected from 20° to 60° 2θ with a step size of 0.01 °2θ at ambient temperature, with pure BFO as a reference in Figure 3-1, and powder peaks were matched with "*Joint Committee on Powder Diffraction Standards"* (JCPDS). In most of the research activites carried out on $BiFeO_3$ it is mentioned that this ceramic has rhombohedral perovskite structure with space group R3c [40], a non-centrosymmetrical structure. Our data is consistent with previous reports and a Rietveld refinement using the R3c space group yields a perfect match with the experimental data. According to Pauling's equation, there is correlation between ionic bond strength I_{AB} with the average electronegativity of cation X_A and anion X_B. As the atomic radius decreases, ionization energy increases and this leads to increases in electronegativity of an atom. The higher the associated electronegativity number, the more an element or compound attracts electrons towards itself. On the other hand, bond energy is a measure of the strength of a chemical bond (the amount of energy (enthalpy) required to be broken), the larger the bond energy, the stronger the bond. Ionic bond strength of La–O (I_{La-O}=799 kJ/mol), Gd–O (I_{Gd-O}=716 kJ/mol) and Sm–O (I_{Sm-O}=619 kJ/mol) bonds are higher than that of Bi–O bond (I_{Bi-O}=343 kJ/mol). This implies that enthalpy of formation ΔH_f of Sm-doped $BiFeO_3$ is more negative as compared to the undoped $BiFeO_3$. More negative enthalpy of formation will lead to more negative free energy of formation ΔG_f of Sm-doped $BiFeO_3$ phase as compared to undoped $BiFeO_3$ phase and possibly compared to secondary phases too, especially at higher temperatures, assisting in improved stability of the perovskite BFO phase upon doping[45]. As we discussed $La^{3+} - O^{2-}$ chemical bond possessed much more stability for the perovskite structure than the $Bi^{3+} - O^{2-}$ chemical bond, minimizing Bi volatilization and reduce the number of O vacancies V_O^{2+}, and consequently stabilizing BFO phase. As a result we can say that by doping BFO with these three elements not only

we are compensating Bi vacancies (V_{Bi}^{3-}) but also we are stabilizing O in its own position which leads to reducing O vacancies (V_O^{2+}). V_O^{2+} comes mainly from V_{Bi}^{3-} and the transition from Fe^{3+} to Fe^{2+}, which can be described by equations (3-1) and (3-2) [79].

$$4Bi^{3+} + 6O^{2-} \rightleftarrows 4Bi_{(gas)} + 3O_{2\ (gas)} + 4V_{Bi}^{3-} + 6V_O^{2+} \qquad (3\text{-}1)$$

$$4Fe^{3+} + 2O^{2-} \rightleftarrows 4Fe^{2+} + O_{2\ (gas)} + 2V_O^{2+} \qquad (3\text{-}2)$$

We also noted substitution with La, Sm and Gd over than 20%, 15% and 12% respectively could lead to secondary phase formation. The desired reaction between Bi_2O_3 and Fe_2O_3 powders is :

$$Bi_2O_3 + Fe_2O_3 \rightarrow 2BiFeO_3 \qquad (3\text{-}3)$$

$$\frac{12}{49}Bi_2Fe_4O_9 + \frac{1}{49}Bi_{25}FeO_{39} \rightleftarrows BiFeO_3 \qquad (3\text{-}4)$$

But it has been reported that secondary phases form due to insufficient reactions between Bi_2O_3 and Fe_2O_3 powders according to the following reaction:

$$Bi_2O_3 + Fe_2O_3 \rightarrow (\frac{2}{x})\ Bi_xFe_yO_{1.5x+1.5y}(x>y) + (\frac{1-y}{x})\ Fe_2O_3\ \text{(unreacted)} \qquad (3\text{-}5)$$

In some samples presence of tiny amounts of Bi_2O_3 were observed around $2\theta = 28°$ (JCPDS 27-0053) which probably is due to excessive Bi used for compensating volatilization during synthesis or unreacted $Bi_2O_3$with melting temperature around 817 °C.

Upon doping with La, Sm or Gd, changes in peaks shapes and positions are observed especially once %5 is exceeded. These changes are more significant for Sm and Gd doped powders as these two have lower ionic radii than La. For both pure BFO and doped powders, our comparative results of the Rietveld refinement of our data are given in Table 3-1. We start our discussion first with the La doped samples as the effect of La doping is relatively weak below 10% contrary to Sm and Gd doped samples. Please note that, where needed, we had to refer to the DTA results of our powders for a reasonable discussion of the XRD and Rietveld results.

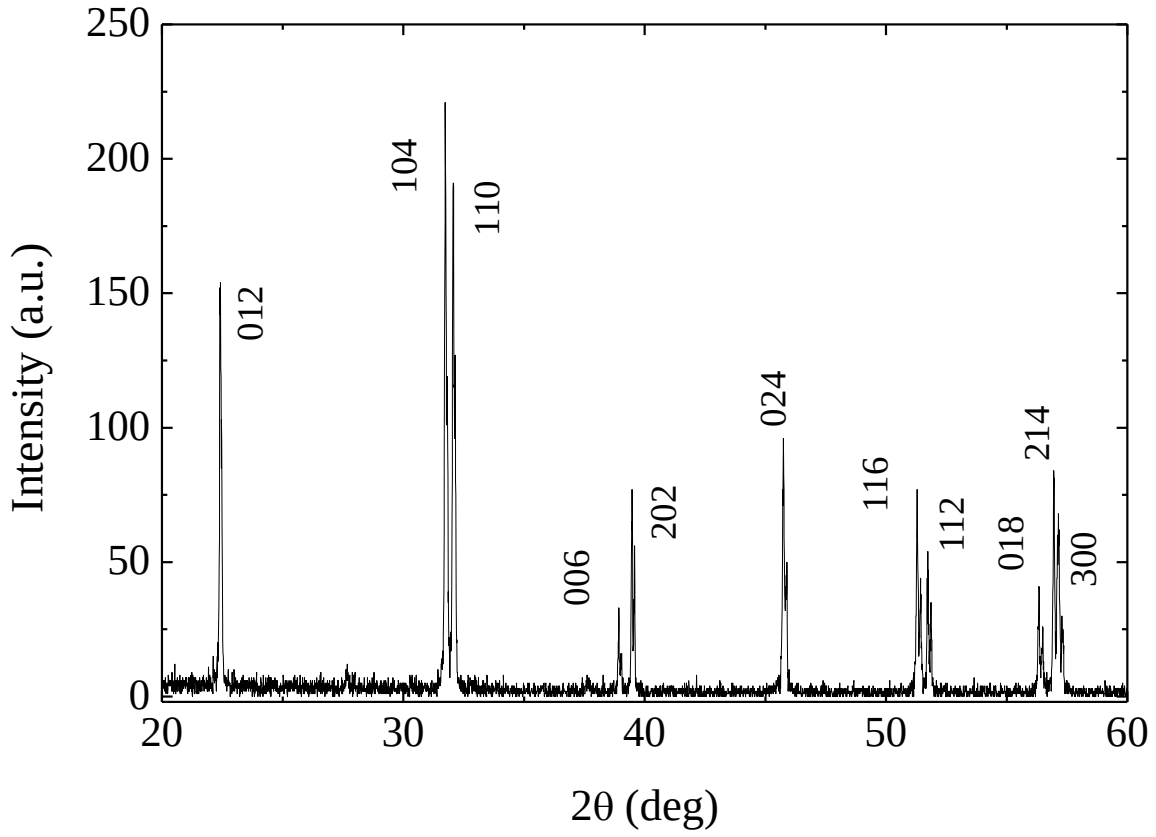

Figure 3-1. XRD Diffraction pattern of the sol-gel synthesized pure $BiFeO_3$ powder in this work.

3.1.1 La doped powders

La doping until around 5% does not have a considerable impact on the XRD peaks where the original BFO peaks and their θ positions are almost conserved (See Figure 3-2a) after which a gradual shift to higher angles start visible only in high resolution as shown for the peaks around 32° in Figure 3-2b. The space group of the La-doped BFO structure appears to be preserved as R3c with the possibility of few percent of Pbnm up after around 10% La doping deduced from the Rietveld refinement where an A-site occupancy ratio as the powder stochiometries we work with was used. Pbnm is a non-polar orthorhombic phase. Polar and anti-polar orthorhombic phases did not reveal better fits than Pbnm in the R3c + Pbnm phase mixtures and therefore we give only the results for the R3c + Pbnm fits in La doped powders in Table 3-1 for brevity. Stability of R3c phase for La ≤10% was also confirmed by our Raman spectroscopy results given in the next section. Similar results have also been reported for the relatively low La doping regime [48-53]. At La concentrations exceeding 10%, we start observing a clear broadening of peaks in the 20°-60° scale accompanied by a slight peak shift towards higher angles, implying an average gradual shrinkage in the unit cells. The peak shift and broadening for the 104-110 planes in high resolution is given in Figure 3-2b. While the peak broadening should be expected due to increased amount of local strain fields around unitcells containing La^{+3} as this ion has around a 1% ionic radius mismatch with Bi^{+3}in 8 coordination within the pseudocubic approximation [54], the gradual merging of peaks above La>10% is consistent with what is reported in [51-53] where an apparent shift toward a higher symmetry structure happens for at least some of the grains as R3c still persists. For La> 10%, our Rietveld refinement fits indicate that Pbnm or Pnma phases, both of which yield a good fit, could be getting stable next to polar R3c where the latter one is still the dominant structure. Pnma is the LaFeO3 space group. In addition, a shrinkage in unitcell volume could be expected to reduce polarization stability due to the restriction of the displacive shift of B-site cation along $[111]_{rhom}$ or $[001]_{hex}$ in the R3c phase along with the loss of the 6s2 lone pairs at La^{+3} sites, weakening the shift of the Fe^{+3} along $[111]_{rhom}$. We found out that La is fully soluble in the BFO lattice even at 20 atomic percent, higher values were reported[43,52,55,56] in powders

Table 3-1. Results of the Rietveld refinement for various phase possibilities. a, b and c are unitcell parameters (GOF: Goodness of the fit)

		R_p'	GOF	Phase Fraction		a(Å)	b(Å)	c(Å)	Unit Cell Volume($Å^3$)
	%0 Gd	5.58	1.00	%100		5.57841	5.57841	13.87210	373.847
	%5 Gd	6.38	1.04	%100		5.57325	5.57325	13.8551	372.70
	%10 Gd	6.21	1.03	%100		5.56334	5.56334	13.8003	369.90
R3c	%15 Gd	8.85	1.34	%100		5.5636	5.5636	13.772	369.19

				R3c%	Pbnm%				
	%0 Gd	5.58	1.00	100	0	5.57825	5.57825	13.87076	373.847
	%5 Gd	6.54	1.03	89.00	11.00	5.5746	5.5746	13.8608	373.03
R3c	%10 Gd	6.30	1.02	82.6	17.4	5.5624	5.5624	13.8041	369.88
+	%15 Gd	7.04	1.11	23.8	76.2	5.554	5.554	13.583	362.8
Pbnm	%15 Gd	7.04	1.11	23.8	76.2	5.6092	5.4290	7.8229	238.23

				R3c%	$Pn2_{(1)}a$%				
	%0 Gd	5.58	1.00	100	0	5.57825	5.57825	13.87076	373.847
R3c	%5 Gd	6.52	1.03	95.8	4.2	5.57356	5.57356	13.8544	372.72
+	%10 Gd	6.48	1.03	97.3	2.7	5.5636	5.5636	13.8027	370.01
$Pn2_{(1)}a$	%15 Gd	6.86	1.08	36.5	63.5	5.5473	5.5473	13.7715	367.00
	%15 Gd	6.86	1.08	36.5	63.5	5.6173	7.8210	5.4360	238.82

	%0 Sm	5.58	1.00	100		5.57841	5.57841	13.87210	373.847
	%5 Sm	6.43	1.05	100		5.57212	5.57212	13.8377	372.079
R3c	%10 Sm	6.20	1.03	100		5.56523	5.56523	13.7936	369.98
	%15 Sm	7.85	1.22	100		5.5569	5.5569	13.661	365.32

					R3c%	*Pbnm%*				
	%0	Sm	5.58	1.00	100	0	5.57841	5.57841	13.87210	373.847
	%5	Sm	6.76	1.05	95.6	4.4	5.57267	5.57267	13.8382	372.17
R3c	%10	Sm	6.00	1.02	86.94	13.06	5.5652	5.5652	13.7970	370.05
+	%15	Sm	7.23	1.14	46.3	53.7	5.5605	5.5605	13.7805	366.81
Pbnm	%15	Sm	7.23	1.14	46.3	53.7	5.4462	5.5935	7.9015	240.70

					R3c%	*$Pn2_{(1)}a$%*				
	%0	Sm	5.58	1.00	100	0	5.57825	5.57825	13.87076	373.847
	%5	Sm	6.65	1.05	98.58	1.42	5.57227	5.57227	13.8397	372.152
R3c	%10	Sm	6.41	1.03	88.7	11.3	5.56543	5.56543	13.7946	370.03
+	%15	Sm	7.70	1.18	72.022	27.978	5.5589	5.5589	13.7922	368.99
$Pn2_{(1)}a$	%15	Sm	7.70	1.18	72.022	27.978	5.6146	7.8271	5.4473	239.39

	%0	La	5.58	1.00	100		5.57825	5.57825	13.87076	373.847
R3c	%5	La	6.24	1.04	100		5.57760	5.57760	13.83963	372.864
	%10	La	6.33	1.04	100		5.57708	5.57708	13.80836	371.952
	%15	La	5.74	1.00	100		5.57777	5.57777	13.7796	371.720

					R3c%	*Pbnm%*				
	%0	La	5.58	1.00	100		5.57825	5.57825	13.87076	373.847
R3c	%5	La	6.34	1.04	97.5	2.5	5.57764	5.57764	13.83967	372.870
+	%10	La	6.34	1.04	98.16	1.84	5.57731	5.57731	13.80923	372.005
Pbnm	%15	La	5.67	1.00	85.2	14.8	5.57732	5.57732	13.7818	371.269

synthesized using various methods and such a high value is possibly emanating from the identical ionic radii of Bi+3 and La+3 for 8 coordination.

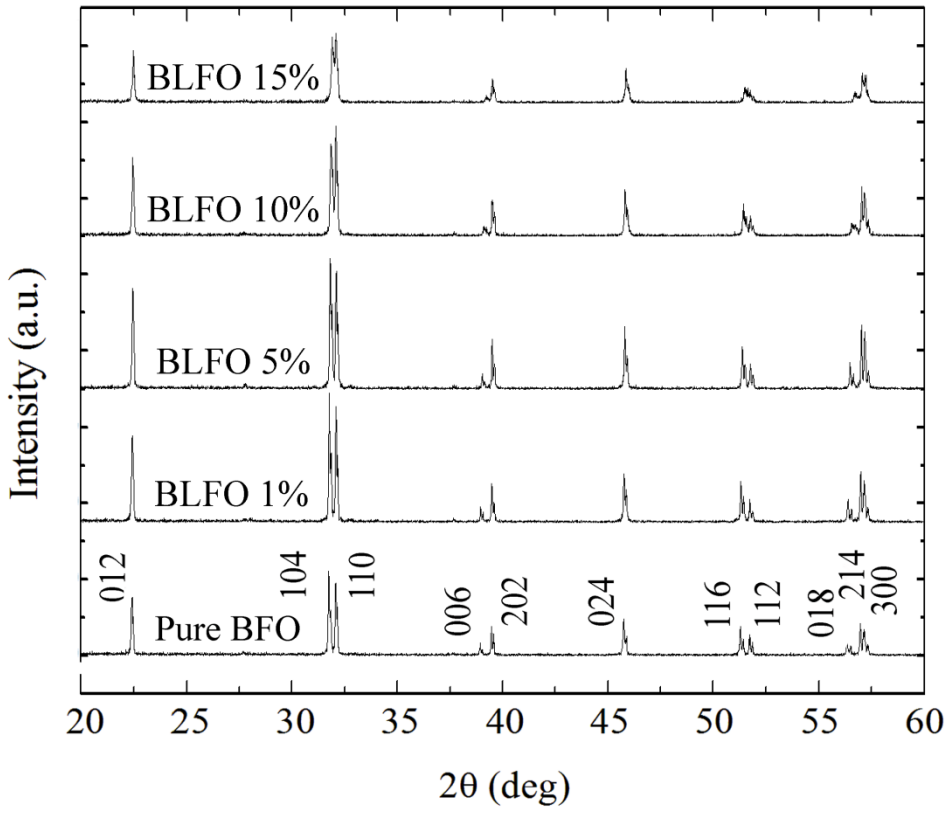

(a)

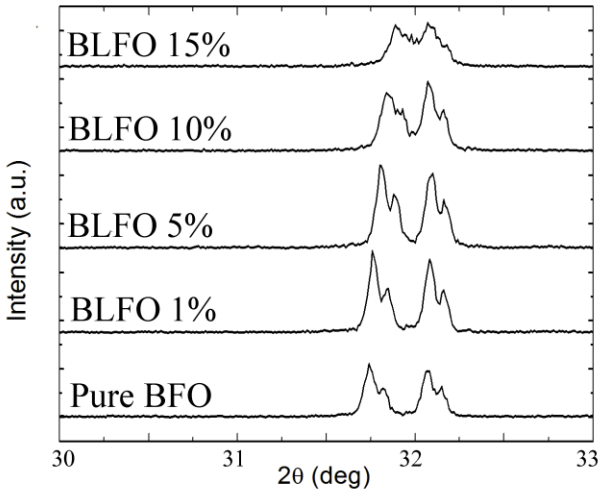

(b)

Figure 3-2. (a) XRD pattern for $Bi_{1-x}La_xFeO_3$ for various concentrations of La and (b) high resolution of the 104 and 110 peaks showing the peak broadening and shift. BLFO: $Bi_{1-x}La_xFeO_3$.

3.1.2 Sm and Gd doped powders

In the case of Sm and Gd doping, the XRD data of powders containing the two dopants are nearly identical despite the fact that Sm+3 in 8 coordination has around 8.5% ionic radius mismatch with Bi+3 and this value for Gd+3 is around 11% obtained from Ref. [54]. In contrast to La, such a difference in the ionic radii of Sm and Gd has an immediate impact on the XRD patterns where, at percentages of Sm and Gd doping 5% and higher, a significant peak broadening together with merging of the double peaks are visible in Figure 3-3a and 3-3b respectively (See Figure 3-4a and Figure 3-4b for the high resolution graph for the 32° range). In our experiments, we find that Sm has a solubility limit of around 15% in BFO while this is nearly 12% for Gd after which non-perovskite impurity phases form. Due to the large ionic radius mismatch of Sm+3 and Gd+3 with Bi+3 for 8 coordination, the grains should be expected to contain a large fraction of inhomogeneous strains around unitcells containing the dopants, causing the highly visible peak broadening along with the possibility of a dopant driven structural change from R3c. The Sm and Gd doped powders have also a lowered transition temperature with respect to La+3 for a given concentration evidenced by our DTA data that is discussed in the next section.

Before going onto the Rietveld analysis discussion of our XRD results for Sm and Gd doped powders, we noted that these samples have considerably smaller grains than pure BFO and La doped BFO up to around 10%, a conclusion we reach after SEM observations (See Figure 3-5). Inhibited diffusion in BFO due to Sm and Gd has been reported previously [42,44,45,57,58], possibly due to reduced amount of vacancies owing to the high enthalpy of Sm-O and Gd-O bonds and the shrinkage of the unitcell. A more than 200% reduction in grain size with respect to pure BFO with higher Sm and Gd dopant concentrations is another possibility to explain peak broadening but cannot directly be held responsible for peak shifts. While this conclusion might appear obvious or even trivial at first, it forms the basis of the discussion for the relation between the observed Curie temperature behavior (discussed in the next section) and the grain sizes making us pose the following question: Are the changes in Curie temperatures due to a size effect in our doped

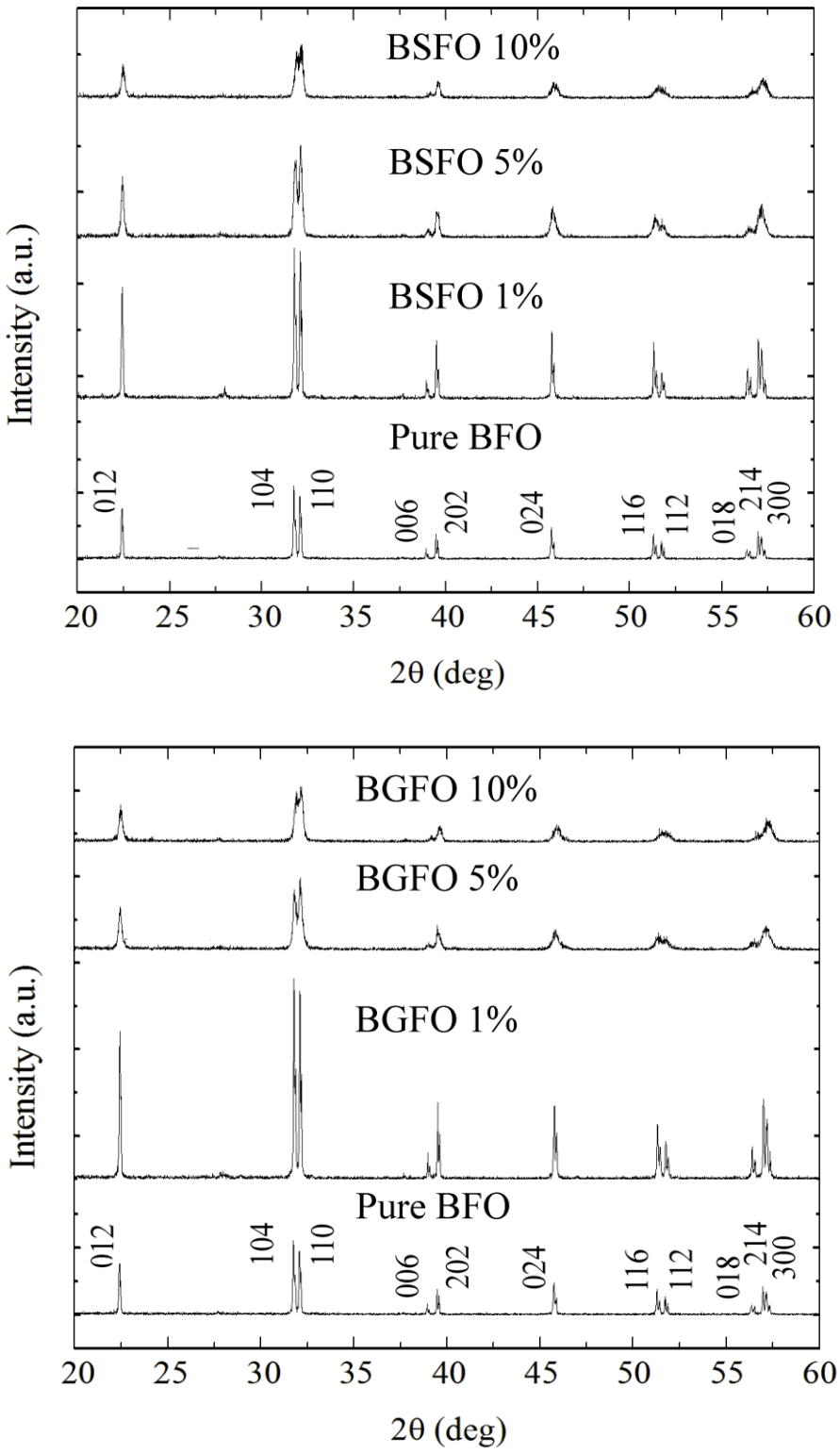

Figure 3-3. . XRD patterns of (Top) Sm doped and (Bottom) Gd doped powders for various concentrations considered in this work

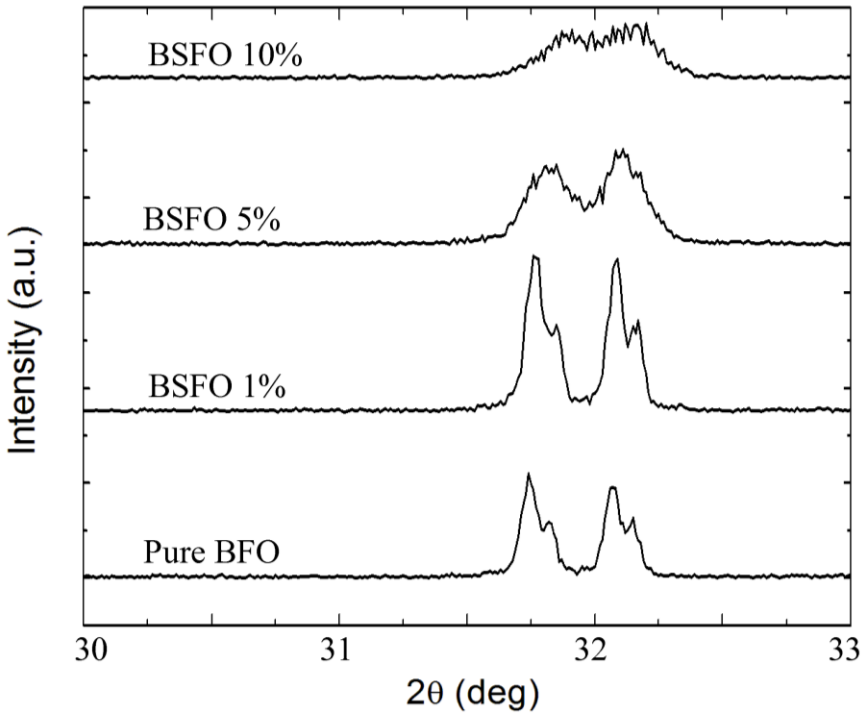

(a)

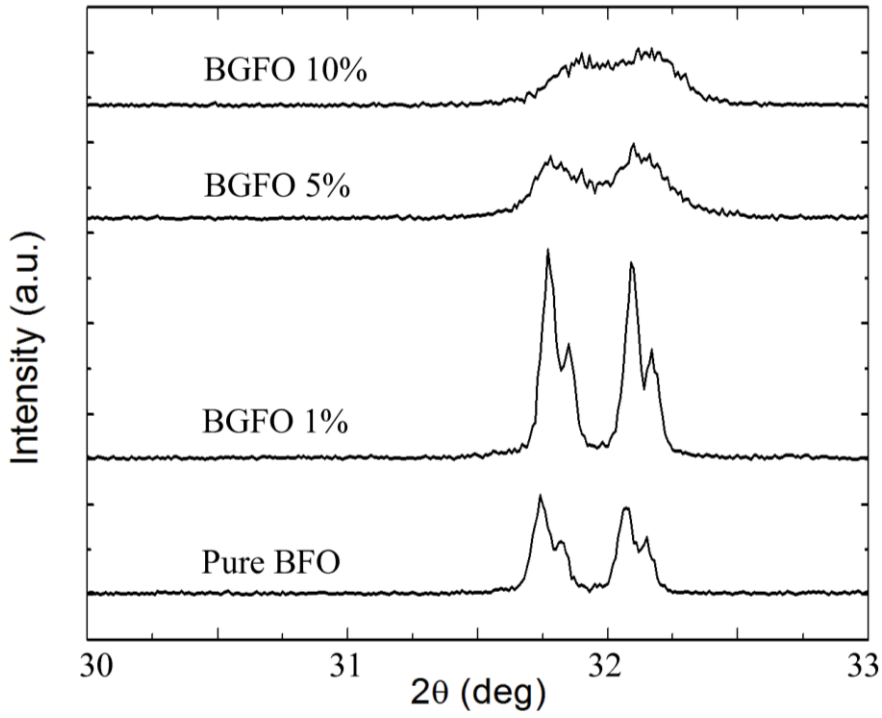

(b)

Figure 3-4. High resolution XRD data around 104-110 peaks are given for (a) Sm and (b) for Gd. BSFO: $Bi_{1-x}Sm_xFeO_3$, BGFO: $Bi_{1-x}Gd_xFeO_3$

powders or is there another mechanism taking effect upon doping Size effects are usually observed in such systems but only at 20-30 nm grain sizes [59-61] while we have grains of about 300 nm or more for heavily doped samples. In fact, Jiaswal et al. has reported that the BFO powders with 50-60 nm particle sizes have only a slightly reduced transition temperature compared to bulk BFO [62]. Therefore, it is likely that our powders are well above the grain size where a size effect could be claimed. Moreover, we see that the change in powder size for Gd and Sm doped samples even after a few percent is negligible, however the reduction of the Curie temperatures depends directly on the dopant radius and concentration.

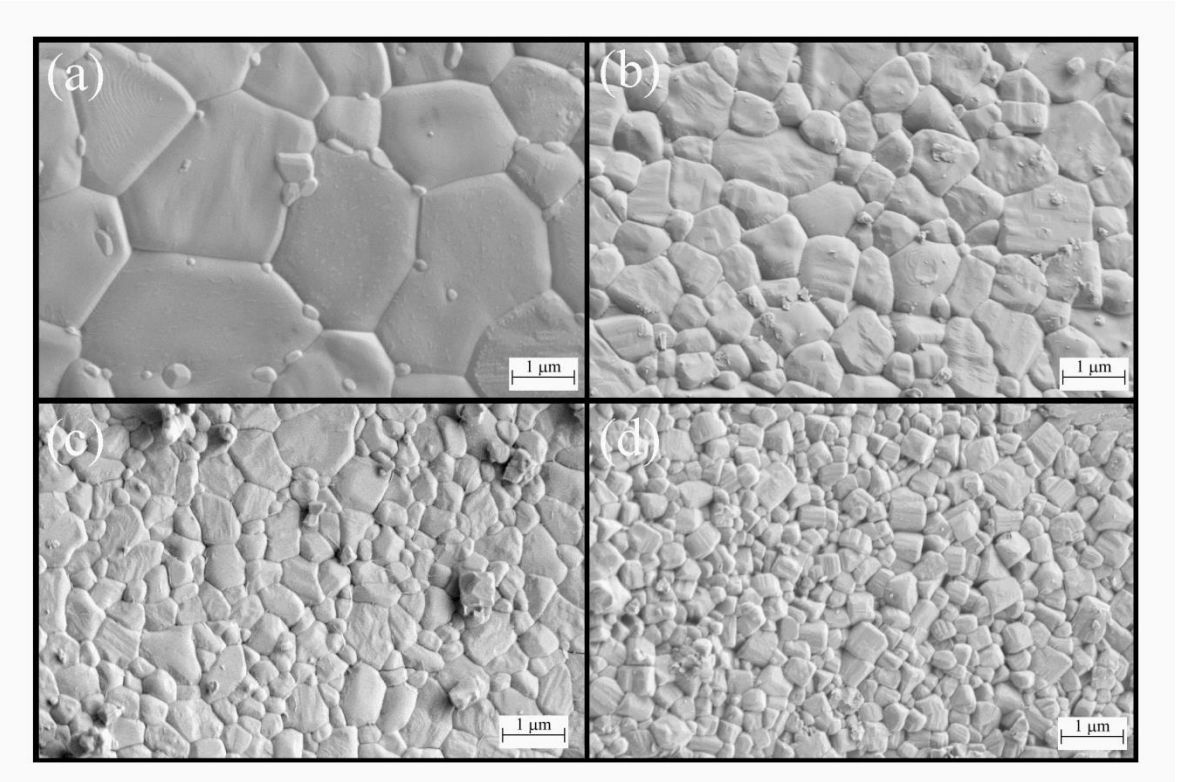

Figure 3-5. SEM image of the synthesized (a) $BiFeO_3$, (b) $Bi_{0.9}La_{0.1}FeO_3$, (c) $Bi_{0.9}Gd_{0.1}FeO_3$and (d) $Bi_{0.9}Sm_{0.1}FeO_3$showing the impact of doping on grain size.

Ruling out a possible size effect, we conclude that the changes in XRD patterns upon doping, in the light of our Rietveld refinement, is a result of significant distortion of the BFO structure upon doping, resulting in parallel stabilization of a phase with higher

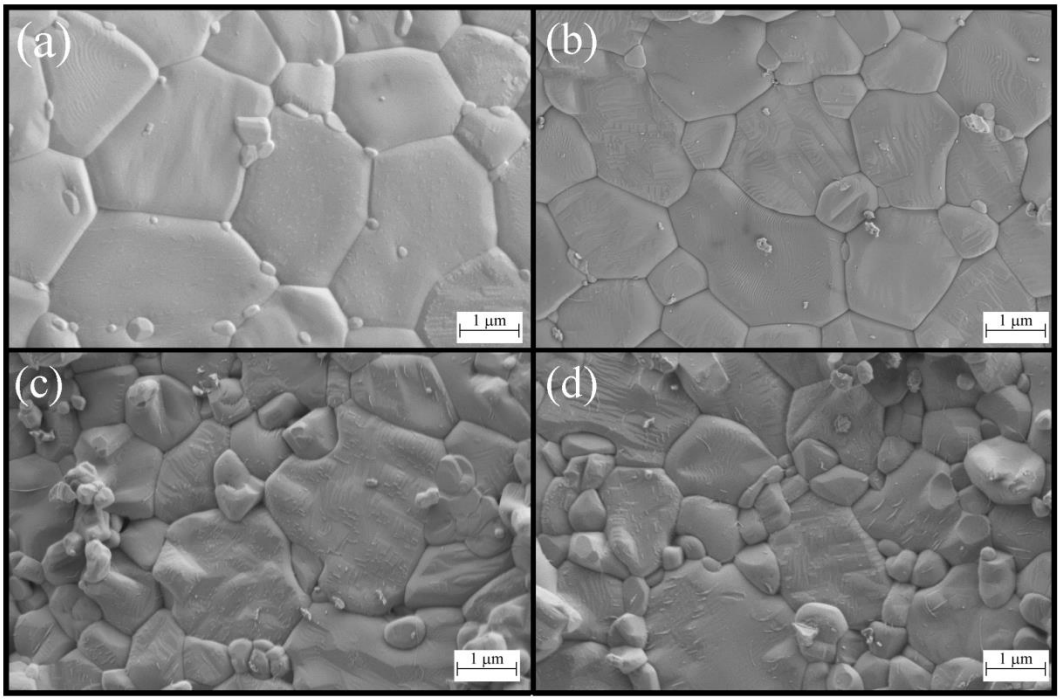

Figure 3-6. SEM image of the synthesized (a) $BiFeO_3$, (b) $Bi_{0.99}La_{0.01}FeO_3$, (c) $Bi_{0.99}Gd_{0.01}FeO_3$and (d) $Bi_{0.99}Sm_{0.01}FeO_3$showing the impact of doping on grain size.

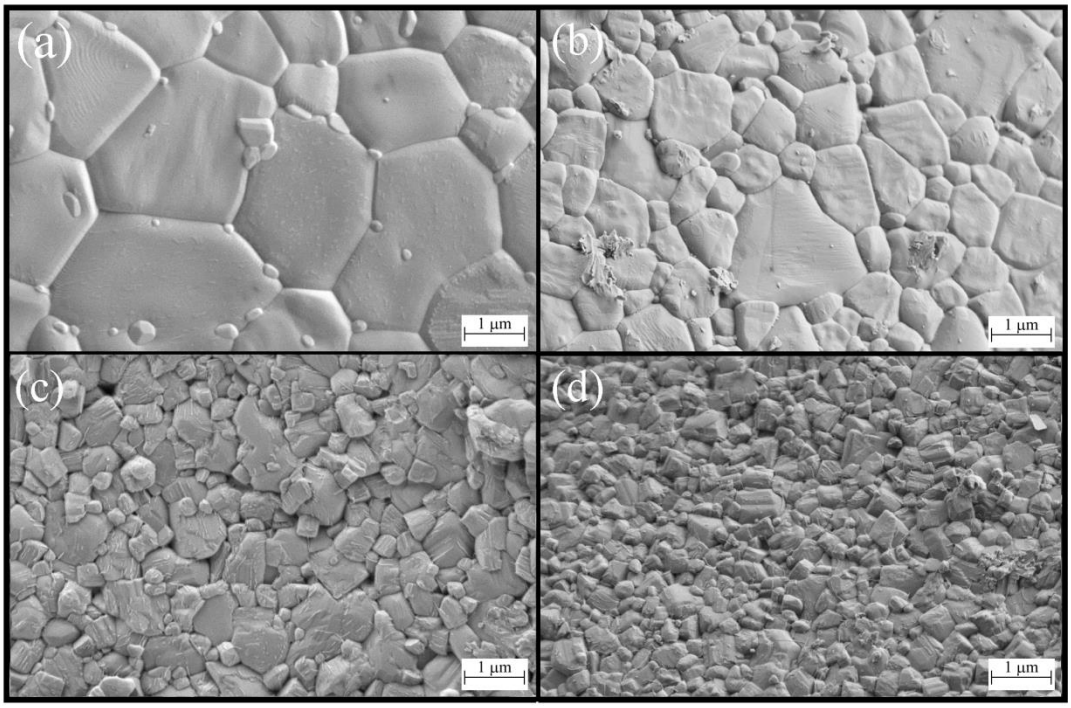

Figure 3-7. SEM image of the synthesized (a) $BiFeO_3$, (b) $Bi_{0.95}La_{0.05}FeO_3$, (c) $Bi_{0.95}Gd_{0.05}FeO_3$and (d) $Bi_{0.95}Sm_{0.05}FeO_3$showing the impact of doping on grain size.

symmetry than R3c along with the R3c itself even at 5% Sm and Gd dopant concentrations. We think so because we obtain the best Rietveld refinement fits to our Sm and Gd doped powders if we consider a orthorhombic (Pbnm) + rhombohedral (R3c) phase mixture following trial runs with P1, C2, Pnma for Sm doped powders and Pn21a as other possible structures reported previously in doped powders: Particularly for Sm and Gd doping concentrations greater than 5%, we can argue that the orthorhombic Pbnm phase around 5-15% (Please see the Rietveld refinement results in Table 3-1) of the total powder volume is stabilized possibly by the chemical pressure induced by dopants along with internal electric fields emanating from inhomogeneous strain fields of these dopants (Discussed in the forthcoming section). From here onwards we insert the * to indicate that the R3c discussed at RT is a distorted structure and call it R3c* with possibly weakened polarity, hence a reduced transition temperature. Regarding Sm doped powders, we get the best fit for Pbnm whereas in Ref. [63], the authors have given a very clear analysis of the La, Sm and Nd doped BFO and report the Pnma phase for Sm as the stable structure at RT. Pnma is antipolar orthoferrite similar to $PbZrO_3$ however the appearance of such an antipolar phase upon cooling from high temperature should yield a signal in the DTA in our 10% and 15% Sm doped powders, similar to what one can expect in PbZrO3 around 231°C, which we do not see in our experiments. The signal we see in 10% Sm doped powders is most likely coming from the PE→R3c* transition of the dopant depleted regions as we get the best fits for a R3c*+Pbnm phase mixture and that the R3c* must have formed above RT (See the detailed discussion in the next section). The authors of Ref. [63] see a DTA peak around 309°C that they attribute to the formation of Pnma, the phase they report at RT, and this could point out the effect of sample preparation technique where they have chosen the solid state calcination method. Similarly, we also found out Pn21a, the polar orthorhombic phase, yields a fit to our Sm and Gd doped powders just as good as or even slightly better than Pbnm for Gd doped samples, a point mentioned in Ref.[47] however lack of any relevant transition peaks in DTA analyses between 900°C and RT (Please see next section) for high concentrations of Sm (≥10%) and Gd (>10%) in our samples led us to choose non-polar Pbnm, which could also be stable at high temperatures in contrast to unlikely existence of polar stability such as the Pn21a which also does not exist at high temperatures

even in pure BFO according to neutron diffraction experiments [64,65]. We revisit this argument for Sm and Gd doped powders in the coming section. The Pbnm phase constitutes a significant volumetric fraction of the grains when the Sm and Gd levels exceed 10% of Bi sites. If we carry out the Rietveld refinement for 15% Gd doped powders, despite the impurity phases appearing in this regime, we find that the samples have more than 79% of its volume in non-polar Pbnm phase, confirming our argument in the light of our DTA data given in the next section. At 15% of Sm doping, we find a phase mixture to enable the best fit between the experiment and Rietveld refinement but with around 54% of Pbnm orthorhombic phase compared to 79% in Gd doped samples with same concentration. Nature of the chemical bonding between dopants and the neighboring oxygen ions have been discussed to effect the ferroelectric distortions for reasons other than the chemical pressure induced by mismatch in ionic radii. The lack of the 6s2 lone pairs in RE elements upon bonding is discussed to be unfavorable for the structural distortions leading to the spontaneous dipole formation in BFO driven by the ionic polarizability degree of freedom of Bi+3. Therefore, that La+3 having an ionic mismatch of only around 1% with Bi+3 under 8 fold coordination causes a small decrease in the Curie temperature can be elaborated from the point of the lack of the stereochemistry that is actually present in Bi+3. However, that this reduction in transition temperature directly scales with the ionic radius mismatch of the A-site dopants with Bi as shown in our work as well as others [63] implies that ionic radius mismatch becomes a stronger contributor to noticeable changes in phase transition temperature and accompanying distortions. For Sm+3 and Gd+3, the effect is most likely due to chemical pressure rather than local chemistry indeed combined with natural formation of internal electric fields owing to the electrostrictive nature of the material keeping in mind that strong internal fields can stabilize centrosymmetric phases with higher symmetry than the polar phase. There is direct correlation between amount of reduction in transition temperatures as will be shown. We try to link the systematically acquired DTA data to the XRD results and define a sequence of phase transitions in our doped powders in the next section.

3.2 Differential Thermal Analysis and Raman Spectroscopy

After determining the crystalline phases via XRD at RT, we carried out DTA experiments to see the effect of dopants on transition temperatures as a function of their ionic radii between RT and 900°C. We do not see any degradation or irreversible dissociation in any of our samples: XRD results at RT before and after DTA remain exactly the same (not shown here). Irreversible dissociation of BFO was reported to occur around 930°C [41] and we stayed under this limit in our experiments. In Figure 3-8, we give the DTA plots of the pure and doped powder samples and in Figure 3-9 the transition temperature (strongest peak) as a function of dopant concentration for the three dopant elements. For 1% doping of La, Sm and Gd, no significant change in high temperature transition is observed and we have a sharp DTA peak in all cases. Therefore, a common result is that 1% doping for all elements has a little impact on the transition temperature of BFO around 820°C and these all appear to be mainly in the R3c phase as confirmed by the Rietveld analysis. 5% and higher concentrations of dopants in powders start to make a difference though: Increasing La occupancy at A-sites induces a gradual reduction in the transition temperature while this reduction is much more rapid for increasing Sm and Gd content. For 5% Sm and Gd doping, the major visible dip indicating a phase transition shifts to much lower temperatures compared to that of 5% La. For 10% Sm and Gd doping, the dips in the DTA curves are at around 400°C and 300°C respectively. Near and beyond the solubility limit of Sm and Gd (15% for Sm and 12% for Gd), we found that doping with 15% Sm and 12% Gd apparently suppresses the transition to below RT in majority of the grains as we observed no indication, i. e. signal, of a transition. On the other hand, 15% La doped powders exhibit the dip at around 530°C, a significantly high temperature with respect to even 10% Sm and Gd containing powder samples. The major visible dip at the transition for doped samples shifting to lower temperatures is accompanied by a strong smearing along with intensity loss with increased dopant content. This smearing and intensity loss is much more profound in Sm and Gd doped samples at 10%. An outcome of this type is often expected in a phase mixture where the dominant phase undergoes no transition while the other may have a transition but with a reduced signal in DTA. Remembering that La doped powders appear to be mostly in the R3c phase and that a Pbnm + R3c* mixture

forms in Sm and Gd doped powders at or above 5%, the weakening of the DTA signal for the case of powder with Sm and Gd >5% might imply that a considerable volume of the grains are in Pbnm phase for the entire temperature range, noticing also that the kink appearing around 800°C also weakens with doping. We discuss the possible origin of this kink in the forthcoming paragraphs.

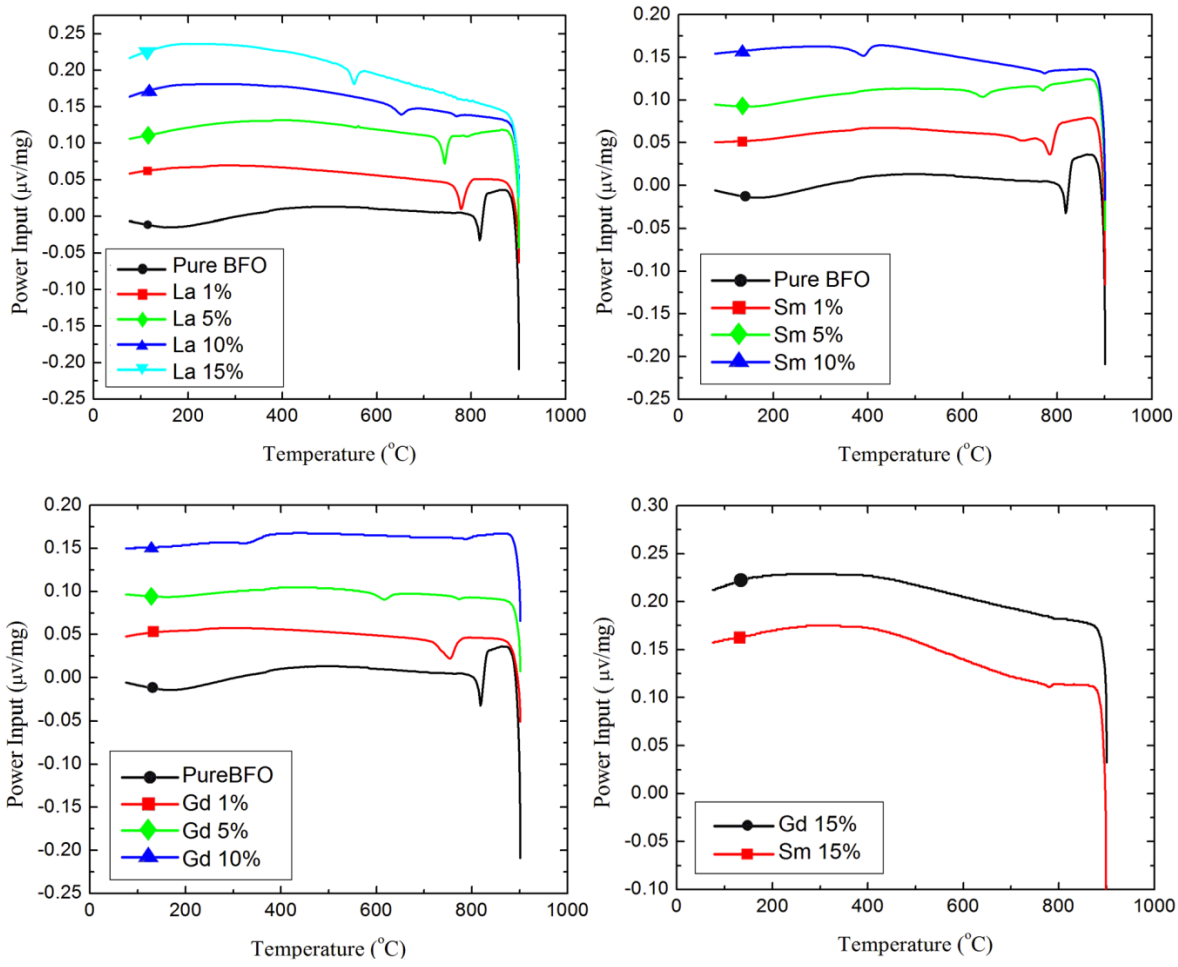

Figure 3-8. DTA curves for pure BFO and various doping levels of $Bi_{1-x}A_xFeO_3$ (A: La, Sm, Gd) samples

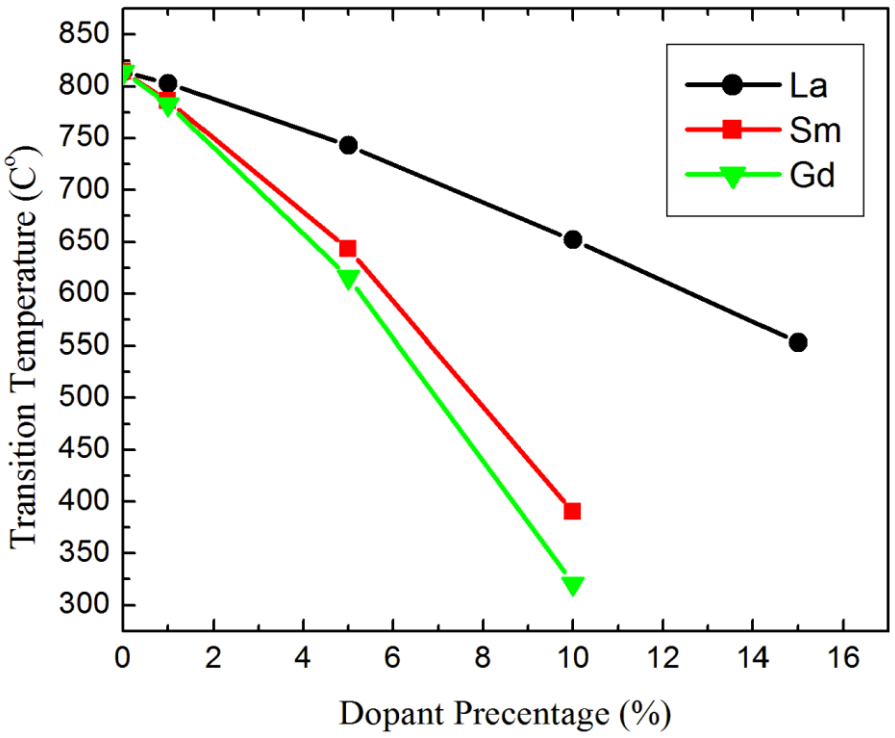

Figure 3-9. Temperature for the possible PE→R3c* transition for doped powders as a function of dopant concentration.

The DTA data can be interpreted in the light of what is observed in the XRD analysis: Increasing the dopant concentration with ions having radii less than Bi+3 reduces the Curie point to lower temperatures concurrent with ionic radius mismatch with Bi+3. Powders with low doping (1%) and are in R3c phase have a transition temperature close to bulk BFO. This trend is still valid for 5% La doped powders. For phase mixtures that appear to be the case for Sm and Gd > 5% and La > 10%, the portion of grains having a lower transition temperature is in the R3c* at RT. The loss of signal intensity in the case of large dopant concentrations indicates that there is a "background" or "parent" phase that does not undergo any transition. This structure is probably the Pbnm phase as any transition from a high temperature PE phase into Pbnm would give a strong peak in DTA, which is not observed in the temperature range considered here. Referring to the previous section, this also helps us to identify the Rietveld refinement fit of the phase mixture as the Pbnm+R3c at RT because we would expect to see a peak in DTA had there been any transition from the paraelectric non-polar Pbnm state to polar P21na phase above RT. In the light of this

argument, larger volumetric fraction of Pbnm phase would mean a greater loss in signal intensity in DTA and this expectation is totally consistet with the case of our doped samples. Moreover, the increase in Pbnm volume fraction appears to be imposing a further reduction of the temperature at which R3c* occurs (because it is present at low amounts in the phase mixture at RT). In the rest of the discussion, we call the non-polar high temperature phase "paraelectric (PE) phase" for sake of generality as there is still some on-going discussion on the structure of this phase in literature and we do not have any precise tools for determining the structure of this phase, which is also outside the scope of our work. The high temperature PE phase has been claimed to have the non-polar P21/m space group symmetry in [46,66] which is probably true for our pure BFO. However, we remind here again that our DTA data combined with the RT XRD results hints at the strong possibility that we might have the non-polar Pbnm phase in heavily doped (>10%) Sm and Gd powders in the entire temperature range of our DTA experiments owing to absence of any peaks above RT but with a small fraction of grains possibly depleted of dopants displaying the regular PE→R3c transition. This transition makes itself visible with the small smeared kink just below 800°C and is independent of dopant type and concentration range considered in this work.

The general reduction of the temperature for the PE→R3c* transition eventually becoming prominent for dopants with smaller ionic radii occurs in grains that are likely to be not in Pbnm phase of the phase mixture when present. This dopant radius dependency can directly be correlated to inhomogeneous lattice strains induced by these dopants in grains which can undergo a PE →R3c* transition. The greater the ionic radius misfit of the dopant with Bi+3 the stronger the reduction of this temperature along with the smearing as observed in our DTA data, keeping in mind again that the presence of the Pbnm phase volume only amplifies this behavior. At 15% doping of both Sm and Gd, we observe no peaks in DTA and this is an expected outcome if one refers to the Rietveld results where the non-polar orthorhombic structure is the dominant volumetric phase at RT. This could indicate that the remaining small R3c volume is also saturated with dopants and has very weak ferroelectricity, hence we call it R3c*, along with a very strong smearing of its

transition and such a mechanism is very well documented in earlier text books on defect effects in phase transition anomalies [67].

We now discuss the all-time presence of the kink in DTA data around 800°C visible in our samples regardless of dopant type and concentration. Such a dip in the DTA curves in the vicinity of the pure BFO Curie point (~820°C) would normally be associated with the PE→R3c transition. For low doping concentrations, no such observation can be claimed as the entire volume appears to be transforming from the parelectric state to ferroelectric relatively close to bulk BFO. At increasing dopant concentrations, this peak or "kink" is relatively easier to distinguish in all our powders despite the fact that it becomes weaker with increased dopant concentration. Such a result points out to a rather inhomogeneous phase transition of the R3c phase in our powders where one can envision the situation of some grains depleted of dopants transforming much earlier than others having inhomogeneous strains due to dopants, for instance during cooling. The remaining fraction is either PE+Pbnm phase mixture that transforms to R3c*+Pbnm upon further cooling or another possibility is PE transforming into R3c*+Pbnm particularly when dopant concentration exceeds 5% (>10% in case of La) as we always find a phase mixture at RT XRD in these cases. We can, however, eliminate PE transforming into R3c*+Pbnm as this would yield either a very strong peak, or at least two peaks at different temperatures in DTA owing to the fact that the appearance of the non-polar Pbnm and polar R3c* phase at the same temperature is very unlikely and neither of it is present in our doped powders.

The decrease of the amplitudes of the 'high temperature' dips in powders with dopant concentrations ≥ 5% for Sm and Gd, >10% for La, indicate that majority of the grains undergo a transition at lower temperatures as can be justified by the relatively stronger, although smeared, intensity of the low temperature peak (around 300-400°C). We think that this is a consequence of strain fields around dopants in grains that can still transform into R3c* from the parent non-polar PE phase. With the amount of such grains decreasing in volume in our powders for higher dopant concentrations, the peak associated with the above transition is expected to weaken and get smeared. In the light of our DTA and XRD data discussed above, the following sequence of transitions can be proposed upon cooling from 900°C to RT in doped samples:

PE phase + Pbnm↓ → R3c^ + Pbnm↓ → R3c* + Pbnm↓ for Sm and Gd ≤ 10% (1)

PE phase + Pbnm↑ → R3c^ + Pbnm↑ → R3c* + Pbnm↑ for Sm and Gd ≥ 15% (2)

where we used ^ to indicate the R3c capable of forming in grains with low dopant concentration having a transition temperature close to bulk BFO, ↓ indicates either "non existing" or "low-to-moderate in volume fraction" and similarly ↑ "high in volume fraction". Sequence given in (2) exhibits no apparent peaks in DTA below 780-800°C (except that the temperature at which the smeared low intensity "kink" exists as with all other powders likely due to a very low fraction of grains exhibiting the PE phase → R3c^ transition) and is probably dominated by the non-polar Pbnm phase, concurrent with the Rietveld refinement. Note that this also signals the possibility that ≥15% Sm and Gd doped powders could be predominantly in Pbnm state at high temperatures and only a small amount of "dopant depleted" grains transform to R3c^ slightly below bulk BFO transition temperature, yielding the relevant weak and smeared but all-time existing kink in DTA. The transitions proposed in (1) is a function of dopant type and concentration for Sm and Gd doped powders as single R3c phase appears to be stable and dominant in La doped powders until around 15%. The visible peaks in DTA associated with transitions in (1) are stronger for low amounts of Pbnm phase if the dopant concentration is not larger than 5%, in particular for Sm and Gd doped samples. Therefore, the strong signal upon the likely transition from the PE phase to R3c* comes from majority of the grains that have almost no Pbnm or low dopant concentration. As described previously, this signal is reduced at high dopant concentrations most likely because of the increased stability and volume fraction of Pbnm and the low amount of R3c* formation in a range of temperatures also leading to smearing of the signal. Note that the peaks we see in the range 300-700°C in 5% or 10% doped samples (See transitions given in 1) cannot be originating from a PE→Pbnm transition because then we would expect to see another peak or kink associated with the Pbnm→R3c* before reaching RT as we find that the RT phase is predominantly R3c* even in 5% Sm and Gd doped BFO following the best Rietveld fits. The structures with high dopant concentration and lower transition temperatures can then be expected to exhibit reduced intensities of Raman scattering according to the given interpretation until now.

This a way to probe ferroelectricity especially in leaky samples like ours where electrical measurements are inconclusive. That the paraelectric-ferroelectric transition of BFO takes place is evident at the expected temperature consistent with previous reports and we now give in Figure 3-10 and 3-11 comparative Raman spectroscopy results of our powders to reveal the effect of dopants on intensity of allowed vibrations of the R3c particularly in the small wave vector regime .

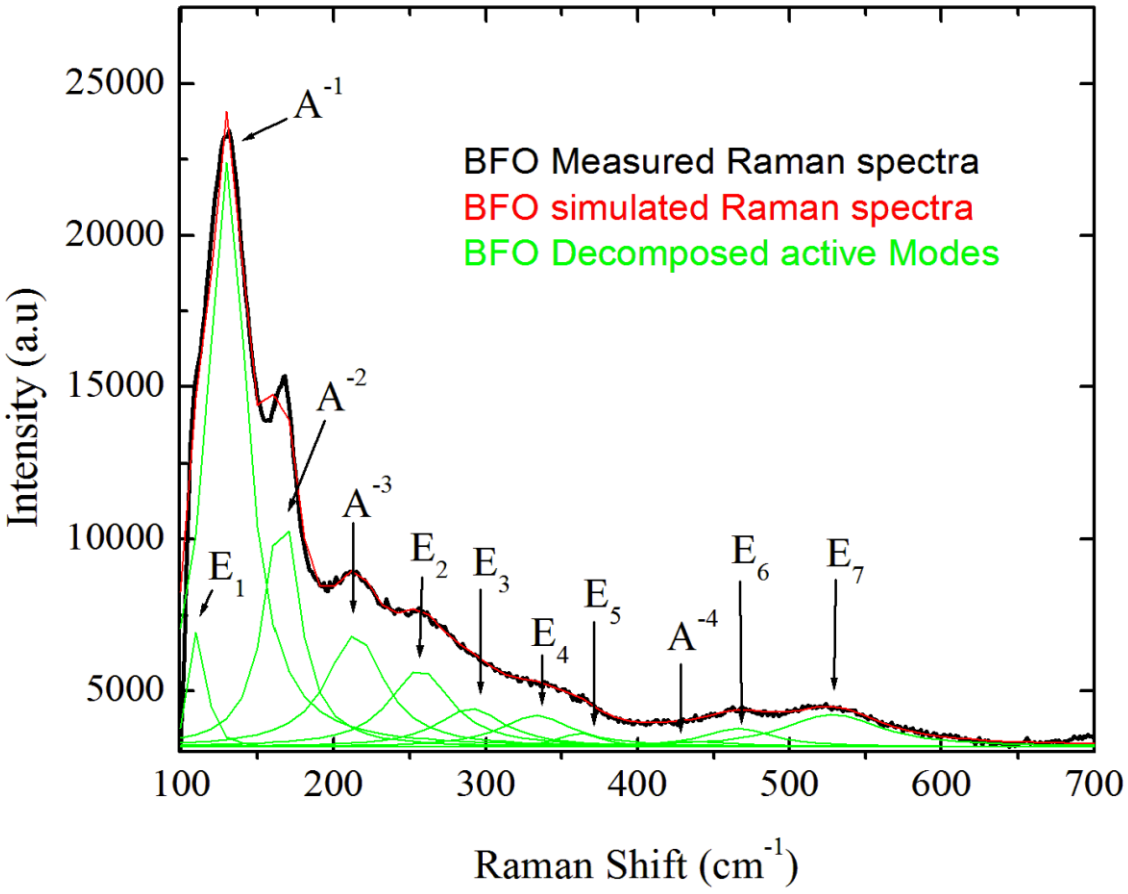

Figure 3-10. Measured Spectra, simulated spectra of the deconvoluted (decomposed) Raman active modes for pure BFO.

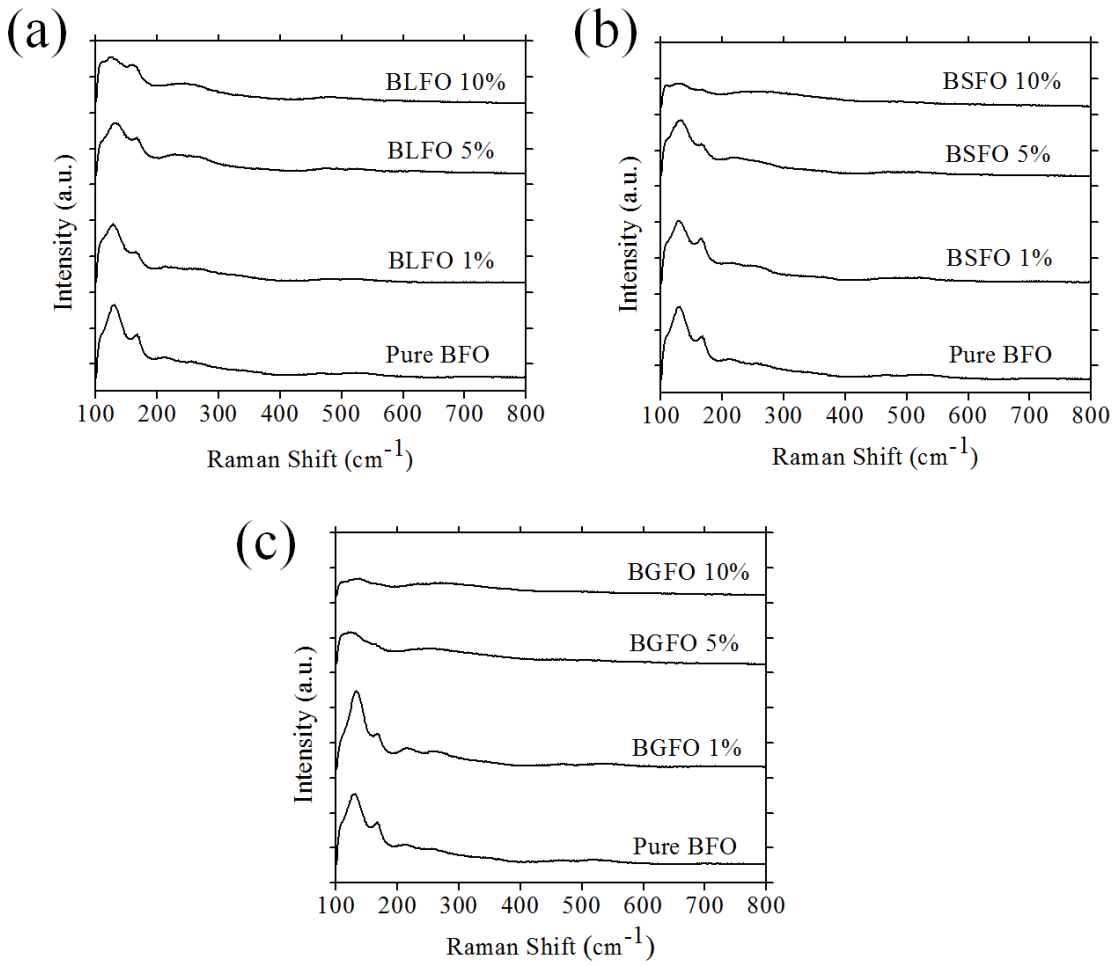

Figure 3-11. Effect of doping on Raman peaks of (a) La doped, (b) Sm doped and (c) Gd doped powders for increasing dopant concentrations. Pure BFO is given in all plots for reference.

Looking at Figure 3-10, the pure BFO exhibits 11 modes of all $4A_1$ + 9E phonon modes that are allowed in the non-centrosymmetrical R3c in part of the spectra until 800 cm-1. The A1 modes are associated with Fe ions and E modes are associated with Bi ions. Raman modes located above 200 cm^{-1} are responsible for distortions and internal vibrations of FeO6 octahedra, and any distortion into the A site of the perovskite enhances the Jahn-Teller distortion of these FeO6 octahedras, while modes below 200 cm^{-1} are attributed to different sites occupied by bismuth inside the perovskite structure. A comparison of Raman peak positions for pure BFO obtained from this study and other works is provided in Table

3-2 for reassurance of the presence of the R3c phase in BFO. Moreover, we noted that the peak positions of nearly all 1% to 5% doped samples coincide with the R3c phase consistent with our XRD results with some visible weakening of intensities in Sm and Gd doped samples.

Table 3-2.Raman modes for R3c BFO in our work and their comparison with other studies.

BFO Raman modes	Yuan et al *2007* [68]	Fukumura et al *2007* [69]	Singh et al *2006* [70]	Present study
A_1^{-1}	126	147	136	129.96
A_1^{-2}	165	176	168	166.47
A_1^{-3}	213	227	211	212.69
A_1^{-4}	425	490	425	419.5
E_1	111.7	-	77	111.44
E_2	259.5	265	275	257.10
E_3	-	279	335	293.5
E_4	339.6	351	365	338.67
E_5	366.9	375	-	365.59
E_6	473.3	437	456	458.75
E_7	599.6	525	597	519.53

In powders containing high concentrations of Sm and Gd (>10%) the R3c modes are very weak or nearly absent as can be seen in Figure 3-11. There is a gradual disappearance of the low frequency modes (large wavelength phonons) upon increased doping concentrations and this is prominent in 5% and 10% Sm and Gd doped powders that exhibit the clear lowering of transition temperatures in the DTA measurements. Thus, the Raman spectra implies a dopant induced “weakening” of the ferroelectric state upon doping of the large mismatch A-site cations. At this point we also sought trace of the Pbnm modes that appear to be the case in Sm and Gd doped powders giving the best Rietveld refinement results consistent with the picture revealed by DTA. In search of the experimental Raman

spectra of the orthorhombic phase, we came across the systematical work of Yang et al. [71] where the orthorhombic phase of BFO was obtained and analyzed in-situ by Raman spectroscopy under high hydrostatic pressure. They observed that intensity of two peaks in the 300-400 cm-1 region was enhanced with increasing hydrostatic pressure that was attributed to FeO6 octahedra tilts. At first sight, it seems reasonable to compare our Raman data to the pressure-induced ortorhombic phase again owing to the fact that the Rietveld results yield the best fit to orthorhombic phase for >%5 Sm and Gd doped powders. We do observe a relative increase in intensity of the modes around 300-400 cm-1 region along with a near-disappearance of low frequency modes of the R3c but because of the inhomogeneous nature of our powders, we can clearly confirm here the disappearance of the R3c modes rather than appearance of the possible Pbnm modes. The inhomogeneous nature of the dopant distribution in our powders is expected to reduce the intensities of the Raman peaks. Although we did not carry out Raman spectroscopy for 15% Sm and Gd doped BFO after observing the almost-total disappearance of R3c peaks in 10% Sm and Gd powders, it is useful to remind here that the Rietveld analysis on this composition has the uncomparably best fit for Pbnm. In another systematic work carried out by Bielecki et al. [53] Tb doped powders (Tb has a very close ionic radius to Gd in 8 coordination) showed a similar trend with the R3c modes rapidly losing intensity after around 10% doping but not a clear signal of the secondary phase was detected despite the mention of a gradual transition upon doping citing precise neutron diffraction studies. The Pnma space group modes in that work, which is claimed to be the phase that the R3c transforms into, started to exhibit themselves only after %17.5 Tb concentrations in the Raman spectra but they also started to see impurity phases such as Bi2Fe4O9 (only in their XRD analysis) which we tried to avoid in our work to reduce complications in data interpretation. It turns out that dopants induce a higher symmetry phase than R3c and the fraction of this phase is a strong function dopant radius. Despite the use of the sol-gel method where homogeneous solutions are prepared, there is strong evidence for “dopant depleted” grains upon crystallization which do undergo a PE→R3c transition but with a tendency of smearing and reduced temperatures depending on dopant radius for a given concentration. It is important to add here that we systematically sought evidence for the inhomogeneous distribution of dopants during SEM sessions as signaled by the DTA results but our efforts were

inconclusive mostly because of submicron grain size. However, with the available structural and thermal analysis data we gathered, we can suggest an apt mechanism using well known phenomena in ferroelectric crystals to explain this interesting result in the next section.

3.2.1 Transition into polar R3c phase from non-polar PE phase in dopant depleted grains

In this section we discuss the shift of the transition peak in DTA to lower temperatures accompanied by a smearing with dopant concentration. Our DTA data implies that, in powders A-site doped at 5% or more, a small fraction of possibly dopant depleted grains still exhibit the PE→R3c^ transition slightly below 820°C with another small fraction of grains exhibiting a reduced transition temperature similarly for the PE→R3c* especially for Sm and Gd doped samples when the doping level less than 15%. We had thought so as the peak associated with any transition gets weaker and smeared with higher dopant concentrations. We already elaborated on the likely possibilities of these transitions but it remains important to understand the origin of the reduction in the temperature for the PE→R3c* transition as a function of dopant radius in some volume of doped powders keeping in mind that our XRD results strongly suggest phase mixtures.

As mentioned previously, transition from one polar symmetry to non-polar or disappearance or weakening of ferroelectric character in BFO (which is mostly due to reduction of the paraelectric-ferroelectric transition) has been often attributed to local bonding changes due to hybridization states between valence electrons and the presence of 6s2 lone pairs, strongly screened from the nucleus of Bi+3 that are absent in rare earth elements such as La, Gd and Sm. Such an effect is also expected to reduce the polarizability of these ions, a driving force often required for distortions leading to ferroelectricity. Despite this often-discussed mechanism, how a few percent of A-site dopants can make a significant reduction in the phase transition temperature of the entire sample remains as a non-trivial question. One must bear in mind that the number of unitcells and therefore the bonds have the same percentage as the dopant concentration. For

instance, in the pseudocubic perovskite structure with 5% dopant concentration, there will be on average about 5 unit cells housing a dopant atom out of 100 unit cells and yet for Sm and Gd doping we observe that there is a considerable reduction in the phase transition temperature accompanied by a clear DTA signal, implying that majority of the structure behaves the same. 5% doped powders that we have yield R3c* as the dominant phase particularly in Sm and Gd doped samples and the shift of the peak position in DTA to lower temperatures is associated with this phase. No such strong reduction is observed in %5 La doped samples. This reduction in transition temperature cannot simply be explained by local bonding chemistry or absence of lone pairs because it is a strong function of dopant radius for a given concentration, keeping in mind the similar valence arrangements and close atomic masses of La, Sm and Gd. With the above picture in sight, we refer to the sensitivity of ferroelectric crystals to inhomogeneous lattice strains to explain the reduction in transition temperature that appears to be dramatically dependent on dopant radius. It is well-understood that any structural inhomogeneity in a ferroelectric crystal is a source of electric field as the Maxwell relation divD=ρ (ρ is space charge due to defects and excitationa across the bandgap and D is dielectric displacement) universally holds in these materials as with any other dielectric. This equation, when expanded and expressed in terms of electrical potential, takes the following form, namely the Poisson equation, considering the ferroelectric polarization components Px, Py and Pz in BFO along [111] direction:

$$\frac{d^2\phi^F}{dx^2}+\frac{d^2\phi^F}{dy^2}+\frac{d^2\phi^F}{dz^2}=\frac{1}{\varepsilon_b\varepsilon_0}\left(\frac{dP_x}{dx}+\frac{dP_y}{dy}+\frac{dP_z}{dz}-\rho\right) \qquad (3)$$

with φ being the electrostatic potential, x, y and z are coordinates in space, Px, Py, Pz are components of ferroelectric polarization vector, ρ is space charge (often called the depletion charge in widebangap materials such as BFO), ε_0 is permittivity of vacuum (8.85×10^{-12}), ε_b is the background dielectric constant, a value on the order of 5-10. The solution of this equation in a random shaped crystallite neighboring others is nearly an impossible task due to the high ambiguity in defining proper boundary conditions both for electrostatic potential and ferroelectric polarization but we can still deduce common sense

implications: One can immediately see from (3) that spatial potential distribution will be a function of the polarization gradients induced by the position dependent strain around the dopant sites that will generate electric fields coupling to the [111] polarization of bulk BFO equal to $(P_x^2 + P_y^2 + P_z^2)^{1/2}$ in magnitude. Even if these gradient variations are less than 1% several unit cells far from the strain source, for instance, it is striking to see that such small variations will scale with $1/\varepsilon_b\varepsilon_0$, a very large number, at the order of 1011. Moreover, due to the large Debye screening lengths (at the order of 10-20 nm, see Ref.[72] which was shown for a formal thin film geometry) even in leaky perovskites, such electric fields will not be screened by free charges and penetrate into a significant volume. Therefore, a random distribution of dopants in the grains, which is the most conservative and natural case to consider, can create random internal electric fields at the order of or higher than coercive field of BFO via their position-wise varying strain fields owing to the electrostrictive nature of the crystal where strain induced polarization is $P_i = (u_{jk} / Q_{ijk})^{1/2}$. Such electric fields emanating from gradual change of polarization, called depolarizing fields, are often present in thin films with imperfect charge screening at film-electrode interfaces [73,74] but the regular and high-symmetry orientation of the entire crystal there helps to naturally develop regular up-down domain patterns to confine the field to the interface, stabilizing ferroelectricity although not in single domain state. In the case of random source distribution of these fields due to distortions around dopants in A-sites within randomly shaped grains, such a mechanism is not possible and one should expect strong internal fields with random direction that can only weaken ferroelectric distortions bearing in mind that random internal fields cannot “enhance” ferroelectricity but only reduce it [67]. The extent of strain field penetration of a point defect such as a dopant is well documented in perovskites and strain fields of such defects extend as much as 4-5 unitcells [75], corresponding to a “volume under influence” consisting of about 125 unit cells. That a large portion of unitcells neighboring a dopant-site will be under the influence of such “inhomogeneous strain driven” internal fields can be concluded even for compositions less than 1 dopant/125 unit cells. BFO grains can then certainly be expected to experience these internal electric fields around dopant sites especially if the ionic radius misfit with Bi+3 is significant, in total accordance with our experimental findings. Large internal depolarizing fields can be capable of suppressing ferroelectricity and therefore

stabilize centrosymmetric phases. It is therefore feasible to expect that a few percent dopant concentrations might stabilize 15-20% Pbnm if the dopant radius misfit with Bi+3 is large. Higher dopant concentrations with "smaller ionic radius" will introduce a larger "distorted volume" distribution and amplify the above mechanism further while low-to-moderate dopant concentrations with radius close to Bi+3 (the case of La) will have a lesser impact as observed in our experiments. Note that dopant induced strains in the case of dopant radius < Bi+3 will not neutralize or cancel each other as sign of strain induced by local displacements will be negative, i. e., pointing towards the strain source that is the dopant itself. A similar effect is documented in ferroelectric crystals with dislocations where the dislocation produces local strain fields that decay away from the core and is a function of Burgers vector magnitude, analogous to the ionic radii mismatch between the dopant and native A-site atom, leading to a degradation [76,77] and smearing [67,78] in ferroelectric properties. It is also well understood that increase in defect density will only degrade polar properties.

We thus have solid evidence that the reduction of the Curie temperature with reduced dopant ionic radius for a given concentration is mainly due to the inhomogeneos strain fields introduced dominating over the mechanism that takes into account the local chemistry of bonds with dopants in the BFO lattice. The effect of RE dopants in BFO is two fold: (i) Dopants with large ionic radii misfit stabilize non-polar phases such as the Pbnm structure, leading to a phase mixture and (ii) the polar phase portion of the phase mixture will experience strong inhomogeneous strains that, via electrostrictive coupling, generate internal electric fields capable of dramatically altering the PE→R3c* temperature, a well understood phenomena in ferroelectric crystals. The sensitivity of the structure and subsequent Curie temperatures being a function of dopant radii can actually be used as a design parameter especially when considering film growth on misfitting substrates. The magnetic substructure of BFO has not been considered as a parameter in discussing changes of the structure as the changes in magnetic ordering at temperatures near RT will be negligible due to the very weak magnetostriction. We also did not see a visible signal to judge as the paramagnetic-antiferromagnetic transition around the reported Neel temperature for pure BFO except a gradual slope change. Moreover, had extensive doping with Gd and Sm been capable of inducing a detectable magnetic transition above RT in

DTA, we would have seen it in ≥ 5% Sm or Gd doped powders, which does not reveal itself. Thus, the detectable peaks in our DTA can be concluded to arise from the structural distortions leading to transitions between various space groups.

Chapter 4. CONCLUSIONS

We studied the effect of A-site dopant radius on the phase transition temperatures and structure of BiFeO3, a magnetoelectric material attracting intense attention. While several works exist in literature on dopant effects, our main point in revisiting dopant effects in BFO was to bring an explanation of the serious impact of dopant radius on phase transition temperatures and lattice structure in the light of experimental data. RT XRD θ-2θ results reveal that the peaks tend to broaden, merge and shift to higher angles faster for dopants with larger ionic radius misfit with Bi+3, implying a shrinkage of the unitcell and a tendency towards a "less distorted rhombohedral" which we named as R3c*. In fact, Rietveld analysis indicate the presence of a R3c* + Pbnm phase mixture for Sm and Gd doped films above 5% and La above 10%, with the Sm and Gd doped powders experiencing the strongest decrease in the transition temperatures. Our DTA data interpreted together with the RT XRD and Raman Spectroscopy results point out to the presence of dopant depletion in some grains because of the all-time present signal in the vicinity of 800°C followed by another signal that shifts faster to lower temperatures accompanied by intensity loss and smearing upon increase in dopant concentration. This shift along with intensity loss and smearing is much stronger in Sm and Gd doped powders. We proposed a sequence of phase transitions that can consistently explain the experimental data and that the Pbnm phase might be the dominant "background" phase in the phase mixtures for high concentration of dopants. Therefore, doping with elements having a smaller ionic radius than Bi+3 can stabilize the Pbnm phase even down to RT with some remnant R3c with a reduced transition temperature. The fraction of "non-Pbnm" grains in doped powders have a reduced PE→R3c transition mostly because of the inhomogeneous strains associated with dopant sites that are still expected to be present. Smaller ionic radius of a dopant creates steeper strain gradients that are capable of creating stronger internal electric fields that is expected to reduce the PE→R3c transition more rapidly along with a strong smearing as also observed in our doped powders. A possible size effect due to inhibited grain growth in doped powders was consistently eliminated as a mechanism behind reduction in the transition temperatures or even disappearance of structural

transitions. Doping with rare earth elements to enhance dielectric and magnetic properties has been a common practice in BFO but our work draws attention to the possible strong impact of structural inhomogeneities and sensitivity of BFO to such formations and that local bonding environments cannot be the sole cause of degradation in ferroelectric behavior. Despite the care shown in preparation of homogeneous precursor solutions, one may end up with inhomogeneous structures with locally varying properties. Comparing our results with that of other groups who have carried out similar experiments with RE dopants but on samples synthesized through a different route, we find rather different phases and phase transition characteristics, pointing out the significance of the synthesis method on properties. We also hope that our results can motivate detailed atomistic computational analysis of dopant effects with particular emphasis on the inhomogeneous strain effects on electronic structure of BFO.

References:

[1] Jeroen and Khomskii, Daniel I Van Den Brink, "Multiferroicity due to charge ordering," Journal of Physics: Condensed Matter, vol. 20, 2008.

[2] Bernhard Keimer, "Transition metal oxides: Ferroelectricity driven by orbital order," Nature Materials, vol. 5, 2006.

[3] Bas B and Palstra, Thomas TM and Filippetti, Alessio and Spaldin, Nicola A Van Aken, "The origin of ferroelectricity in magnetoelectric YMnO3," Nature materials, vol. 3, 2004.

[4] Ho Nyung and Christen, Hans M and Chisholm, Matthew F and Rouleau, Christopher M and Lowndes, Douglas H Lee, "Strong polarization enhancement in asymmetric three-component ferroelectric superlattices," Nature, vol. 433, 2005.

[5] Ronald E Cohen, "Origin of ferroelectricity in perovskite oxides," Nature, vol. 358, 1992.

[6] Mamontov, E and Egami, T and Dmowski, W and Gog, T and Venkataraman, C Mamontov, "Anisotropic covalent bonds in KNbO3 observed by resonant X-ray scattering," Physical Review B, 2002.

[7] VS Pokatilov, AS Sigov, and AO Konovalova, "NMR and Mössbauer study of multiferroic BiFeO3," Bulletin of the Russian Academy of Sciences: Physics, vol. 74, 2010.

[8] P. Curie, J. "Sur la symétrie dans les phénomènes physiques, symétrie d'un champ électriglue et d'un champ magnétique" Physique 3, 393, 1894.

[9] Filippetti A and Hill N.A, "Coexistence of magnetism and ferroelectricity in perovskites," Phys. Rev. B, vol. 65, 2002.

[10] Lebeugle D, A D. Colson, and M. Viret, Forget, "Room-temperature coexistence of large electric polarization and magnetic order in BiFeO3 single crystals," Phys. Rev. B, vol. 76, 2007.

[11] Yao Wang, Jiamian Hu, Yuanhua Lin, and Ce-Wen Nan, "Multiferroic magnetoelectric composite nanostructures," NPG Asia Materials, 2010.

[12] Meiya Li, Min Ning, Yungui Ma, Qibin Wu, and CK Ong, "Room temperature ferroelectric, ferromagnetic and magnetoelectric properties of Ba-doped BiFeO3 thin films," Journal of Physics D: Applied Physics, 2007.

[13] GL and Or, SW and Wang, YP and Liu, ZG and Liu, JM Yuan, "Preparation and multi-properties of insulated single-phase BiFeO3 ceramics," Solid state communications, 2006.

[14] C. de la Vega, Ma.E. Fuentes and L. Fuentes, "BiFeO3: Synchrotron radiation structure refinement and magnetoelectric geometry," Journal of the European Ceramic Society, 2007.

[15] JBNJ and Neaton, JB and Zheng, H and Nagarajan, et al. Wang, "Epitaxial BiFeO3 multiferroic thin film heterostructures," Science, 2003.

[16] Qing-Hui and Nan, Ce-Wen and Shen, Zhi-Jian Jiang, "Synthesis and Properties of Multiferroic La-Modified BiFeO3 Ceramics," Journal of the American Ceramic Society, 2006.

[17] R. et al. Haumont, "Phonon anomalies and the ferroelectric phase transition in multiferroic BiFeO," Physical Review B, 2006.

[18] A and Francois, M and Gachon, JC Maitre, "Experimental study of the Bi2O3-Fe2O3 pseudo-binary system," Journal of Phase Equilibria and Diffusion, 2004.

[19] R and Katiyar, et al. Palai, "β phase and γ-β metal-insulator transition in multiferroic BiFeO3," Physical Review B, 2008.

[20] Igor A. et al. Kornev, "Finite-Temperature Properties of Multiferroic BiFeO," Physical review letters, 2007.

[21] M. et al. Thrall, "An in situ study of the formation of multiferroic bismuth ferrite using high resolution synchrotron X-ray powder diffraction," Journal of the European Ceramic Society, 2008.

[22] M NAGAO, M OKUYAM KY YUN, "Prominent ferroelectricity of BiFO3 thin films prepared by pulsed-laser deposition," Appl Phys Lett, 2003.

[23] Zhigang and Cohen, Ronald E Wu, "Pressure-Induced Anomalous Phase Transitions

and Colossal Enhancement of Piezoelectricity in PbTiO3," *Physical review letters*, 2005.

[24] J. Nogues and I. K. Schuller, "Exchange bias," Journal of Magnetism and Magnetic Materials, 1999.

[25] Ying-Hao. et al. Chu, "Electric-field control of local ferromagnetism using a magnetoelectric ," Nature materials, 2008.

[26] et al. H Béa, "Ferroelectricity down to at least 2 nm in multiferroic BiFeO3 epitaxial thin films," Japanese journal of applied physics, 2006.

[30] JF. et al. Scott, "Properties of ceramic KNO3 thin-film memories," Physica B+ C, 1988.

[31] K. Yoshokawa, N. Okada K. Ishikawa, "Size effect on the ferroelectric phase transition in PbTiO3 ultrafine particles," Phys. Rev. B, 37, 1988.

[32] I. P. and Wurfel, P. and Silverman, B. D Batra, "New Type of First-Order Phase Transition in Ferroelectric Thin Films," Phys. Rev. Lett., 1973.

[33] H. Ikawa, Ceramic Transactions, 1993.

[34] Sergei V Kalinin and Et al, "Potential and impedance imaging of polycrystalline BiFeO3 ceramics," Journal of the American Ceramic Society, vol. 85, 2002.

[35] V. R. et al PALKER, "Magnetoelectricity at Room Temperature in the Bi(0.9-x)Tb(x)La(0.1)FeO3 System," Phys. Rev, 2004.

[36] Q. H. JIANG, C. W. NAN, and Z. J. SHEN, "Synthesis and properties of multiferroic la modified BiFeO3 ceramics," Journal of the American Ceramic Society, 2006.

[37] M. Valant, A. Axelsson, and N. Alford, "Peculiarities of a solid-state synthesis of multiferroic polycrystalline BiFeO3," Chemistry of Materials, 2007.

[38] KIM, J. K.; KIM, S. S.; KIM, W. J. Sol-gel synthesis and properties of multiferroic BiFeO3. Materials Letters, 2005.

[39] KUMAR, M. M. et al. Ferroelectricity in a pure BiFeO ceramic. Applied Physics Letters, v. 76, p. 2764, 2000.

[40] J. M. Moreau, C. Michel, R. Gerson, W. J. James, “Ferroelectric BiFeO3 X-ray and neutron diffraction study” J. Phys. Chem. Solids 1971, 32, 1315.

[41] Catalan, G. and J.F. Scott, Physics and Applications of Bismuth Ferrite. Advanced

Materials, 2009. 21(24): p. 2463-2485.

[42] Pradhan, S.K., et al., Defect driven multiferroicity in Gd doped BiFeO3 at room temperature. Journal of Magnetism and Magnetic Materials, 2010. 322(22): p. 3614-3622.

[43] Simoes, A.Z., F.G. Garcia, and C.D. Riccardi, Rietveld analysys and electrical properties of lanthanum doped BiFeO3 ceramics. Materials Chemistry and Physics, 2009. 116(2-3): p. 305-309.

[44] Lotey, G.S. and N.K. Verma, Structural, magnetic, and electrical properties of Gd-doped BiFeO3 nanoparticles with reduced particle size. Nanoparticle Research, 2012. 14(3).

[45] Nalwa, K.S. and A. Garg, Phase evolution, magnetic and electrical properties in Sm-doped bismuth ferrite. Journal of Applied Physics, 2008. 103(4).

[46] Haumont, R., et al., Phase stability and structural temperature dependence in powdered multiferroic BiFeO(3). Physical Review B, 2008. 78(13).

[47] Khomchenko, V.A., et al., Effect of Gd substitution on the crystal structure and multiferroic properties of BiFeO3. Acta Materialia, 2009. 57(17): p. 5137-5145.

[48]Cheng, Z.X., et al., Structure, ferroelectric properties, and magnetic properties of the La-doped bismuth ferrite. Journal of Applied Physics, 2008. 103(7).

[49] Le Bras, G., et al., Magnetization and magnetoelectric effect in Bi1-xLaxFeO3 (0 <= x <= 0.15). Physical Review B, 2009. 80(13).

[50] Lan, C.Y., Y.W. Jiang, and S.G. Yang, Magnetic properties of La and (La, Zr) doped BiFeO3 ceramics. Journal of Materials Science, 2011. 46(3): p. 734-738.

[51] Zhang, Q., et al., Effect of La3+ substitution on the phase transitions, microstructure and electrical properties of Bi1-xLaxFeO3 ceramics. Journal of Alloys and Compounds, 2013. 546: p. 57-62.

[52] Rusakov, D.A., et al., Structural Evolution of the BiFeO3-LaFeO3 System. Chemistry of Materials, 2011. 23(2): p. 285-292.

[53] Bielecki, J., et al., Structural and magnetic properties of isovalently substituted multiferroic BiFeO3: Insights from Raman spectroscopy. Physical Review B, 2012.

86(18).

[54] Shannon, R.D., Revised Effective Ionic Radii and Systematic Studies of Interatomic Distances in Halides and Chalcogenides. Acta Crystallographica, 1976. A32: p. 751-767.

[55] Zhang, S.T., et al., Substitution-induced phase transition and enhanced multiferroic properties of Bi1-xLaxFeO3 ceramics. Applied Physics Letters, 2006. 88(16).

[56] Garcia, F.G., C.S. Riccardi, and A.Z. Simoes, Lanthanum doped BiFeO3 powders: Syntheses and characterization. Journal of Alloys and Compounds, 2010. 501(1): p. 25-29.

[57] Singh, P., et al., Correlation of microstructure and electrical conduction behaviour with defect structure of niobium doped barium stannate. Journal of Alloys and Compounds, 2007. 437(1-2): p. 34-38.

[58] Dai, H.Y., et al., Microstructure and properties of Sm-substituted BiFeO3 ceramics. Journal of Rare Earths, 2012. 30(11): p. 1123-1128.

[59] Akdogan, E.K., et al., Size effects in PbTiO3 nanocrystals: Effect of particle size on spontaneous polarization and strains. Journal of Applied Physics, 2005. 97(8).

[60] Akdogan, E.K. and A. Safari, Thermodynamic theory of intrinsic finite-size effects in PbTiO3 nanocrystals. I. Nanoparticle size-dependent tetragonal phase stability. Journal of Applied Physics, 2007. 101(6).

[61] Akdogan, E.K. and A. Safari, Thermodynamic theory of intrinsic finite size effects in PbTiO3 nanocrystals. II. Dielectric and piezoelectric properties. Journal of Applied Physics, 2007. 101(6).

[62] Jaiswal, A., et al., Temperature-Dependent Raman and Dielectric Spectroscopy of BiFeO3 Nanoparticles: Signatures of Spin-Phonon and Magnetoelectric Coupling. Journal of Physical Chemistry C, 2010. 114(29): p. 12432-12439.

[63] Karimi, S., et al., Crystal chemistry and domain structure of rare-earth doped BiFeO3 ceramics. Journal of Materials Science, 2009. 44(19): p. 5102-5112.

[64] Arnold, D.C., et al., Ferroelectric-Paraelectric Transition in BiFeO3: Crystal Structure of the Orthorhombic beta Phase. Physical Review Letters, 2009. 102(2).

[65] Arnold, D.C., et al., The beta-to-gamma Transition in BiFeO3: A Powder Neutron

Diffraction Study. Advanced Functional Materials, 2010. 20(13): p. 2116-2123.

[66]Palai, R., et al., beta phase and gamma-beta metal-insulator transition in multiferroic BiFeO3. Physical Review B, 2008. 77(1).

[67] Sigov, A.P.L.a.A.S., Defects and structural phase transitions. Ferroelectricity and related phenomena, ed. Taylor W. Vol. 6. 1988: Gordon and Breach.

[68] Yuan, G.L., S.W. Or, and H.L.W. Chan, Raman scattering spectra and ferroelectric properties of Bi1-xNdxFeO3 (x=0-0.2) multiferroic ceramics. Journal of Applied Physics, 2007. 101(6).

[69] Fukumura, H., et al., Raman scattering study of multiferroic BiFeO3 single crystal. Journal of Magnetism and Magnetic Materials, 2007. 310(2): p. E367-E369.

[70] Singh, M.K., et al., Polarized Raman scattering of multiferroic BiFeO3 epitaxial films with rhombohedral R3c symmetry. Applied Physics Letters, 2006. 88(4).

[71] Yang, Y., et al., High pressure Raman investigations of multiferroic BiFeO3. Journal of Physics-Condensed Matter, 2009. 21(38).

[72] Misirlioglu, I.B. and M. Yildiz, Dielectric response of fully and partially depleted ferroelectric thin films and inversion of the thickness effect. Journal of Physics D-Applied Physics, 2013. 46(12).

[73]Bratkovsky, A.M. and A.P. Levanyuk, Abrupt appearance of the domain pattern and fatigue of thin ferroelectric films. Physical Review Letters, 2000. 84(14): p. 3177-3180.

[74] Chensky, E.V. and V.V. Tarasenko, THEORY OF PHASE-TRANSITIONS TO INHOMOGENEOUS STATES IN FINITE FERROELECTRICS IN AN EXTERNAL ELECTRIC-FIELD. Zhurnal Eksperimentalnoi I Teoreticheskoi Fiziki, 1982. 83(3): p. 1089-1099.

[75] Carpenter, M.A., et al., Characteristic length scale for strain fields around impurity cations in perovskites. Physical Review B, 2009. 80(21).

[76] Chu, M.W., et al., Impact of misfit dislocations on the polarization instability of epitaxial nanostructured ferroelectric perovskites. Nature Materials, 2004. 3(2): p. 87-90.

[77] Alpay, S.P., et al., Can interface dislocations degrade ferroelectric properties? Applied

Physics Letters, 2004. 85(11): p. 2044-2046.

[78] Skulski, R. and P. Wawrzala, The results of computerized simulation of the influence of dislocations on the degree of phase transition diffusion in BaTiO3. Physica B, 1997. 233(2-3): p. 173-178.

[79] Yu, Benfang and Li, Meiya and Liu, Jun and Guo, "{Effects of ion doping at different sites on electrical properties of multiferroic BiFeO3 ceramics". Journal of Physics D: Applied Physics, 2008, p. 065003.